JEM Journal of Experimental Medicine

ARTICLE

LINGO4 coordinates ILC3-intrinsic IL-22 production and microbiota-mediated ILC3 homeostasis

José L. Fachi[1*], Tihana Trsan[1*], Cristiane Sécca[1], Sarah de Oliveira[1,2], Vinícius R. Rodovalho[3], Patrick Fernandes Rodrigues[1], Wandy L. Beatty[4], Raki Sudan[1], Shitong Wu[1], Bishan Bhattarai[1], Santosh K. Panda[1], Marina Cella[1], Susan Gilfillan[1], and Marco Colonna[1]

LINGO4 is a leucine-rich repeat and immunoglobulin-like domain-containing transmembrane protein encoded immediately adjacent to *Rorc*, the gene for RORγt, raising the possibility that it contributes to the biology of RORγt⁺ lymphocytes. However, its impact on these cells and resistance to enteric infections has remained unknown. Here, we identify LINGO4 as a critical regulator of group 3 innate lymphoid cells (ILC3s). *Lingo4*$^{-/-}$ ILC3s exhibit a profound, cell-intrinsic defect in IL-22 production linked to impaired STAT3 activation, mitochondrial dysfunction, elevated ROS, and increased apoptosis. *In vivo*, *Lingo4* deficiency also drives a dysbiotic gut microbiota, resulting in an additional, microbiota-dependent loss of ILC3s. These combined defects increase susceptibility to *Clostridioides difficile* and *Citrobacter rodentium*, whereas IL-22 reduction in *Lingo4*$^{-/-}$ mice confers protection against *Salmonella typhimurium*. Immunoprecipitation of tagged LINGO4 reveals interaction networks enriched in mitochondrial pathways, providing mechanistic insight into its role in ILC3 metabolic fitness and intestinal immunity.

Introduction

Innate lymphoid cells (ILCs) are a family of lymphocytes that lack antigen-specific receptors yet parallel the effector functions of T helper (Th) cell subsets (Eberl et al., 2015; Klose and Artis, 2016; Vivier et al., 2018). Unlike T cells, ILCs do not undergo antigen receptor rearrangement and therefore respond rapidly to environmental cues without requiring antigen recognition, priming, or clonal expansion (Vivier et al., 2018). Among mucosal tissues, the intestine contains the highest density of ILCs, where they serve as early sentinels that integrate signals from dietary metabolites, stromal and epithelial cells, and the resident microbiota (Li et al., 2018; Wang et al., 2023; Faria et al., 2017; Klose and Artis, 2016).

Group 3 ILCs (ILC3s), defined by expression of the transcription factor RORγt and production of IL-22 and IL-17, are central to maintaining intestinal barrier integrity (Cella et al., 2009; Sanos et al., 2009; Eberl et al., 2004; Cupedo et al., 2009; Satoh-Takayama et al., 2008; Gury-BenAri et al., 2016). IL-22 produced by ILC3s drives epithelial proliferation, antimicrobial peptide release, and resistance to enteric pathogens, while IL-17 contributes to neutrophil recruitment and mucosal immunity (Horn and Sonnenberg, 2024; Reynders et al., 2011; Sabihi et al., 2020; Cupedo et al., 2009; Liang et al., 2006). ILC3s also shape the composition and spatial organization of the gut microbiota, and their development and effector functions are strongly influenced by microbial metabolites, including aryl hydrocarbon receptor (AHR) ligands, tryptophan metabolites, and short-chain fatty acids (SCFA) (Chun et al., 2019; Fachi et al., 2020; Fachi et al., 2025; Kiss et al., 2011; van de Pavert et al., 2014; Lehmann et al., 2020; Grizotte-Lake et al., 2018; Lee et al., 2011). Through these reciprocal interactions, ILC3s function at the interface of host defense and microbial ecology, and perturbations in ILC3 activity can profoundly alter susceptibility to infection, inflammation, and dysbiosis.

ILC3 identity and function are maintained by a core transcriptional program centered on RORγt and AHR, which together regulate ILC3 survival, metabolic fitness, and IL-22 production (Sun et al., 2000; Eberl et al., 2004; Lee et al., 2011; Serafini et al., 2015; Sawa et al., 2010; Lo et al., 2019). Leucine-rich repeat and immunoglobulin-like domain-containing protein 4 (LINGO4) is a transmembrane protein composed of an extracellular ectodomain containing multiple leucine-rich repeats capped by cysteine-rich regions followed by an immunoglobulin-like domain, a single transmembrane segment, and a short cytoplasmic C-terminal tail. LINGO4 is encoded immediately adjacent to the *Rorc* locus and is robustly expressed in RORγt⁺ lineages, including ILC3s and Th17 cells, suggesting coordinated regulation with RORγt and RORγ

[1]Department of Pathology and Immunology, Washington University in St. Louis, School of Medicine, Saint Louis, MO, USA; [2]Department of Genetics, Evolution, Microbiology, and Immunology, Institute of Biology, University of Campinas, Campinas, Brazil; [3]Bioinformatics Laboratory, National Laboratory for Scientific Computation (LNCC), Petrópolis, Brazil; [4]Department of Molecular Microbiology, Washington University in St. Louis, School of Medicine, Saint Louis, MO, USA.

*J.L. Fachi and T. Trsan contributed equally to this paper. Correspondence to Marco Colonna: mcolonna@wustl.edu; José L. Fachi: fachijl@wustl.edu.

(He et al., 1998; Sun et al., 2000). Prior studies of LINGO4 have focused largely on neuronal development (Haines and Rigby, 2008; Guillemain et al., 2020), leaving unknown whether and how LINGO4 influences mucosal immunity or the function of RORγt⁺ lymphocytes.

Here, we show that LINGO4 is a critical regulator of ILC3 homeostasis and effector function. Deletion of *Lingo4* results in a cell-intrinsic defect in ILC3 activation, characterized by reduced IL-22 production, impaired STAT3 phosphorylation, mitochondrial dysfunction, and increased apoptosis. In contrast, the numerical reduction of ILC3s in *Lingo4*$^{-/-}$ mice is largely microbiota dependent, reflecting an extrinsic defect shaped by altered microbial communities and host–microbiota interactions. Consistent with the IL-22 role in host defense, *Lingo4*-deficient mice are more susceptible to *Clostridioides difficile* and *Citrobacter rodentium* pathogens controlled by IL-22-dependent epithelial immunity but are more resistant to *Salmonella enterica* serovar Typhimurium, for which IL-22 instead promotes pathogen expansion. Together, these findings identify LINGO4 as a previously unrecognized regulator of mucosal immunity that maintains ILC3 fitness, IL-22 production, and host–microbiota homeostasis.

Results

Lingo4 deficiency impairs ILC3 numbers and function

Since *Lingo4* is encoded immediately adjacent to *Rorc*, which encodes RORγt, we first asked whether its expression is coordinated with RORγt⁺ lymphocytes. Analysis of publicly available ImmGen ATAC-seq datasets (Heng et al., 2008) revealed that immune populations with accessible chromatin at the *Rorc* locus also showed accessibility at the *Lingo4* locus (Fig. S1 A), consistent with shared regulatory control. Examination of ImmGen transcriptional datasets across immune subsets further revealed that *Lingo4* expression closely mirrors *Rorc* expression, with transcripts detected specifically in RORγt-expressing populations but not early hematopoietic progenitors (Fig. S1, B and C). This pattern suggests that *Lingo4* co-expression with *Rorc* is established at the stage of RORγt⁺ lineage specification. Among RORγt-expressing lymphocytes, *Lingo4* transcript levels were highest in ILC3 subsets, with lower expression in splenic γδ T cells and thymic double-positive T cells (Fig. S1 C). We validated these findings by RT-quantitative PCR (qPCR) using sort-purified ILC3s, CD4⁺ T cells, CD8⁺ T cells, and γδ T cells from multiple tissues, confirming that ILC3s express the highest levels of *Lingo4* (Fig. S1, D–H). Sorting RORγt⁺ and RORγt⁻ cells from *Rorc*^{GFP} reporter mice further demonstrated that *Lingo4* expression is enriched in RORγt⁺ ILC3s, supporting its potential relevance for ILC3 biology (Fig. S1 I). These observations provided the rationale for generating *Lingo4*-deficient mice to directly assess its function.

Global deletion of *Lingo4* resulted in a reduction of ILC3s in the small intestinal (si) lamina propria (LP) (siLP), whereas colonic ILC3s were unaffected (Fig. 1, A–C). Among ILC3 subsets (NKp46⁺, CCR6⁺, and double-negative [DN] ILC3s), the CCR6⁺ and DN populations were proportionally reduced in siLP but not in colon (Fig. 1, D and E). RORγt⁺ Th17 and RORγt⁺ pTreg cells were similarly reduced in the siLP, with no differences observed in the colon (Fig. S1, J and K). The ILC3 deficit persisted in *Rag1*$^{-/-}$, *Tcrb*$^{-/-}$, and *Tcrd*$^{-/-}$ backgrounds (Fig. S1, L–N), indicating that the phenotype does not arise from altered T cell compartments. Because RORγt is essential for ILC3 lineage identity (Sun et al., 2000; Eberl et al., 2004), we asked whether LINGO4 influences its expression. RORγt protein levels were comparable between WT and *Lingo4*$^{-/-}$ ILC3s (Fig. 1 F), demonstrating that the reduction in ILC3 numbers is not caused by impaired lineage specification. Functionally, *Lingo4*$^{-/-}$ siLP ILC3s exhibited reduced IL-22 production, both at steady state and following IL-23 stimulation (Fig. 1 G). IL-17 production was only modestly affected after IL-23 stimulation, whereas IFN-γ, TNF-α, and GM-CSF were unchanged (Fig. 1 G and Fig. S1 O). IL-22 and IL-17 were comparably reduced across all three siLP ILC3 subsets (Fig. 1 H and Fig. S1 P). The expression of IL-23R was comparable between genotypes (Fig. S1 Q), indicating that reduced cytokine production is unlikely to reflect impaired IL-23 sensing or ligand binding, though downstream signaling defects cannot be excluded. Similarly to the siLP, colonic *Lingo4*$^{-/-}$ ILC3s showed impaired IL-22 production at baseline and after IL-23 stimulation, whereas IL-17 production was reduced only following stimulation (Fig. 1 I).

To distinguish intrinsic from extrinsic requirements for *Lingo4*, we generated mixed bone marrow chimeras by reconstituting CD45.1 recipients with equal proportions of WT (CD45.1/CD45.2) and *Lingo4*$^{-/-}$ (CD45.2) donor cells (Fig. 1 J). In this competitive environment, *Lingo4*$^{-/-}$ ILC3s showed only a modest reduction in reconstitution, indicating that the decrease in ILC3 abundance is only minimally cell intrinsic (Fig. 1 K). In sharp contrast, *Lingo4*$^{-/-}$ ILC3s retained a pronounced defect in IL-22 production even when developing in the same host as WT ILC3s (Fig. 1 L), demonstrating a strong, cell-intrinsic requirement for LINGO4 in IL-22 production. Reconstitution of CD4⁺ and CD8⁺ T cells remained normal (Fig. S1 R). To determine whether the ILC3 defect in *Lingo4* mice depends on *Lingo4* expression in ILC3s rather than in T cells, which also express *Lingo4*, we crossed *Lingo4*$^{fl/fl}$ mice with *Serinc2*^{iCre} (Rodrigues et al., 2025), generating *Lingo4*$^{\Delta ILC3}$ conditional KOs, in which *Lingo4* is deleted in ILC3s but spared in Th17 cells. *Lingo4*$^{\Delta ILC3}$ mice partially phenocopied the global KO, displaying reduced ILC3 numbers, predominantly within the DN subset (Fig. 1, M and N), and diminished IL-22 production, whereas IL-17 production remained intact (Fig. 1 O). Because *Serinc2* is also expressed in the epithelial cells (Rodrigues et al., 2025), we performed RT-qPCR analysis of intestinal epithelial cells from WT mice and did not detect *Lingo4* expression (Fig. S1 S), suggesting that the observed phenotype in *Serinc2*^{iCre} mice is ILC3 specific. Together, these results indicate that LINGO4 exerts a dual role in ILC3 biology. The impairment in IL-22 production is predominantly cell intrinsic and occurs independently of T cells or altered RORγt expression. By contrast, the reduction in ILC3 numbers reflects a modest intrinsic contribution coupled to a substantial extrinsic component.

ILC3 abundance in *Lingo4*$^{-/-}$ mice is microbiota dependent

ILC3 abundance is shaped by both cell-intrinsic programs and extrinsic signals from the intestinal microbiota, including food-

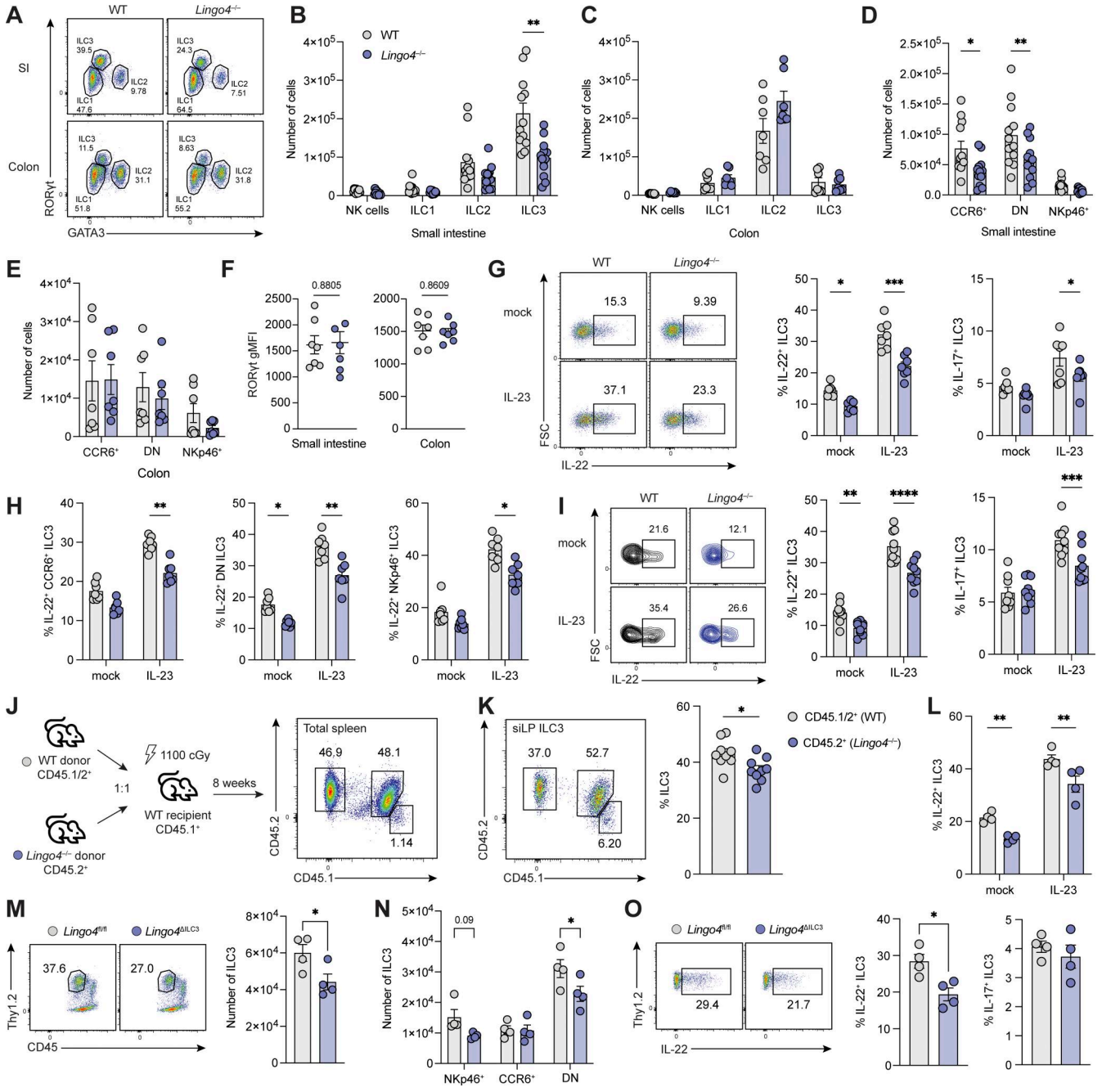

Figure 1. **LINGO4 deficiency reduces ILC3 abundance and IL-22 production in a cell-intrinsic manner. (A–C)** Representative flow cytometry plots (A) and absolute numbers of ILCs in the si (B) and colonic (C) LP of WT and *Lingo4*$^{-/-}$ mice. Mean ± SEM, *n* = 7–12; pooled from three independent experiments. **(D and E)** Numbers of ILC3 subsets (NKp46^{+}, CCR6^{+}, and DN) in the siLP (D) and colon (E) of WT and *Lingo4*$^{-/-}$ mice. Mean ± SEM, *n* = 7–12; pooled from four experiments. **(F)** Geometric mean fluorescence intensity (gMFI) of RORγt in ILC3s from siLP and colon of WT and *Lingo4*$^{-/-}$ mice. Mean ± SEM, *n* = 6–7; two experiments combined. **(G)** Representative flow cytometry plots and frequencies of IL-22^{+} and IL-17^{+} siLP ILC3s after *ex vivo* stimulation with IL-23 (10 ng/ml). Mean ± SEM, *n* = 7; two experiments combined. **(H)** Frequencies of IL-22^{+} cells across siLP ILC3 subsets after *ex vivo* stimulation with IL-23. Mean ± SEM, *n* = 7; two experiments combined. **(I)** Representative flow cytometry plots and frequencies of IL-22^{+} and IL-17^{+} colonic ILC3s after *ex vivo* stimulation with IL-23 (10 ng/ml). Mean ± SEM, *n* = 9; two experiments combined. **(J)** Mixed BM chimeras: irradiated CD45.1 recipients (1,100 cGy) were reconstituted with a 1:1 mixture of CD45.1/2^{+} WT and CD45.2^{+} *Lingo4*$^{-/-}$ BM cells. Representative reconstitution profile in spleen at 8 wk. *n* = 9; two experiments combined. **(K and L)** Frequencies of WT (CD45.1/2^{+}) and *Lingo4*$^{-/-}$ (CD45.2^{+}) ILC3s in siLP (K) and IL-22^{+} ILC3s following IL-23 stimulation (L). Mean ± SEM, *n* = 9 (K) and *n* = 4 (L); two experiments combined. **(M and N)** Representative flow cytometry plots and numbers of ILC3s (M) and ILC3 subsets (N) in siLP of *Lingo4*$^{fl/fl}$ and *Lingo4*$^{\Delta ILC3}$ mice. ILC3s were defined as live lymphocyte-sized Lin^{-} (CD3^{-} CD19^{-}) Thy1.2^{hi} CD45^{int} cells. Mean ± SEM, *n* = 4; representative of two experiments. **(O)** Frequencies of IL-22^{+} and IL-17^{+} ILC3s after IL-23 stimulation. Mean ± SEM, *n* = 4; representative of two experiments. **(A–O)** Statistical significance was assessed using unpaired two-tailed *t* tests or one-way ANOVA with Tukey's post hoc test. *P < 0.05; **P < 0.01; ***P < 0.001; ****P < 0.0001.

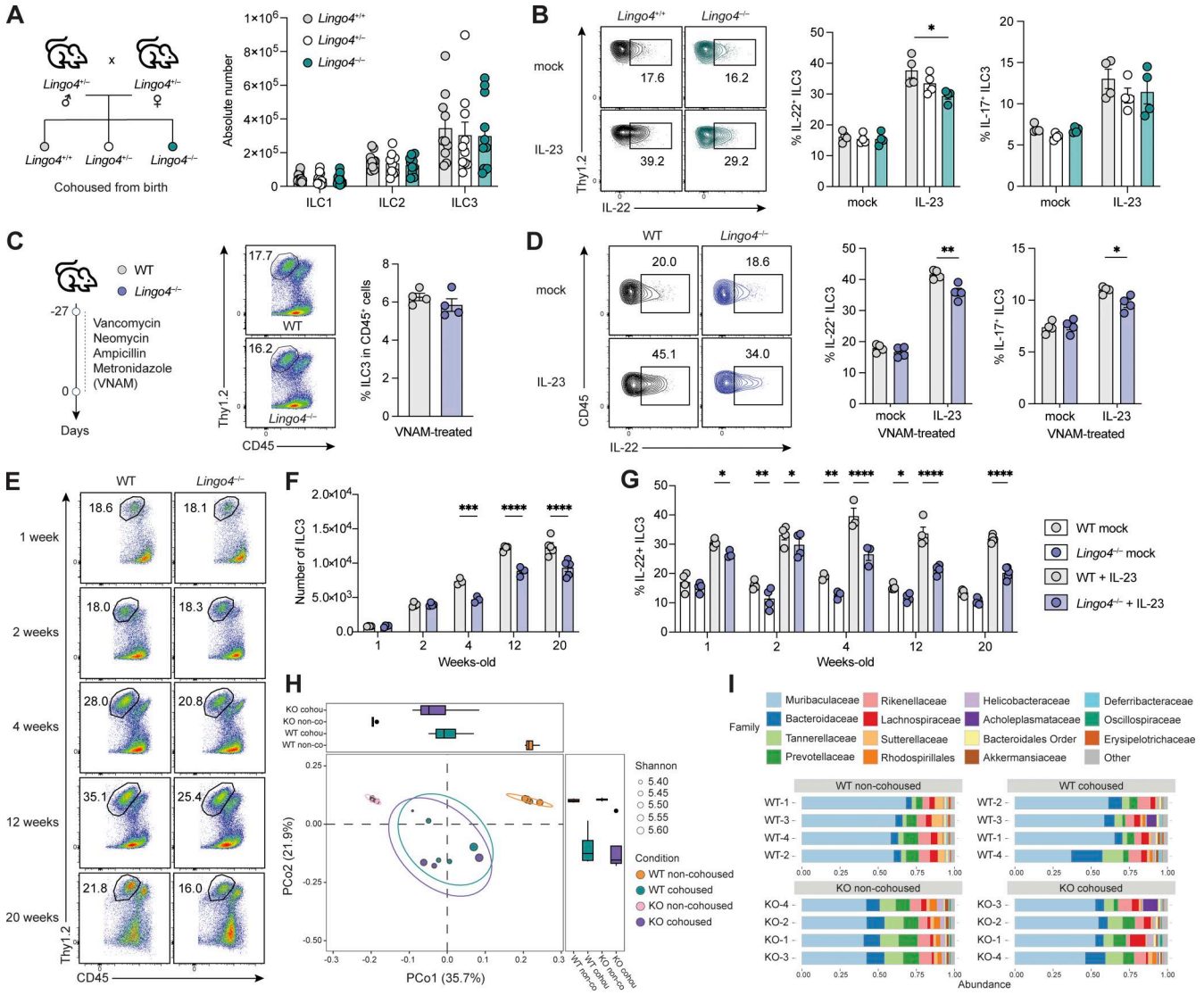

Figure 2. **Reduced ILC3 responses in *Lingo4*$^{-/-}$ mice depend on gut microbiota. (A)** Numbers of ILCs in siLP of cohoused *Lingo4*$^{+/+}$, *Lingo4*$^{+/-}$, and *Lingo4*$^{-/-}$ littermates. Mean ± SEM, *n* = 9–11; three experiments combined. **(B)** Representative flow cytometry plots and frequencies of IL-22^{+} and IL-17^{+} ILC3s after IL-23 stimulation. Mean ± SEM, *n* = 4; representative of three experiments. **(C and D)** Antibiotic depletion of microbiota. VNAM treatment scheme and frequencies of ILC3s in non-cohoused VNAM-treated WT and *Lingo4*$^{-/-}$ mice (C). IL-22^{+} and IL-17^{+} ILC3s after IL-23 stimulation (D). ILC3s were defined as live lymphocyte-sized Lin^{-} (CD3^{-} CD19^{-}) Thy1.2^{hi} CD45^{int} cells. Mean ± SEM, *n* = 4; representative of two experiments. **(E–G)** Representative plots (E), numbers of ILC3s (F), and IL-22^{+} ILC3 frequencies following IL-23 stimulation (G) in WT and *Lingo4*$^{-/-}$ mice at different ages. ILC3s were defined as live lymphocyte-sized Lin^{-} (CD3^{-} CD19^{-}) Thy1.2^{hi} CD45^{int} cells. Mean ± SEM, *n* = 4–5. **(H and I)** Fecal microbiota composition analysis of cohoused and non-cohoused WT and *Lingo4*$^{-/-}$ mice. Principal coordinates analysis (PCoA) of Bray–Curtis distances showing β diversity; dot size indicates α diversity (Shannon index) (H). Relative abundance at the family level (I). *n* = 4. **(A–G)** Statistical significance was assessed using unpaired two-tailed *t* tests or one-way ANOVA with Tukey's post hoc test. *P < 0.05; **P < 0.01; ***P < 0.001; ****P < 0.0001.

derived metabolites such as SCFAs and AHR ligands (Gury-BenAri et al., 2016; Horn and Sonnenberg, 2024). To determine whether microbiota-dependent mechanisms contribute to the reduced ILC3 numbers in *Lingo4*$^{-/-}$ mice, we first cohoused WT, *Lingo4*$^{+/-}$, and *Lingo4*$^{-/-}$ littermates from birth. Under these conditions, the difference in ILC3 numbers was completely normalized (Fig. 2 A), indicating that the numerical defect is not solely cell intrinsic but strongly influenced by the microbial environment. In contrast, although steady-state IL-22 and IL-17 production were comparable across genotypes (Fig. 2 B), IL-23 stimulation revealed a selective and persistent defect in IL-22, but not IL-17, production in *Lingo4*$^{-/-}$ ILC3s. This finding indicates that IL-22 defect is microbiota independent and strictly cell intrinsic. To further distinguish intrinsic from extrinsic requirements for *Lingo4*, we performed reciprocal bone marrow transfers between WT and *Lingo4*$^{-/-}$ hosts (Fig. S2 A). *Lingo4*$^{-/-}$ donor cells showed incomplete ILC3 reconstitution even in WT hosts, demonstrating a cell-intrinsic defect in the ability of *Lingo4*$^{-/-}$ progenitors to generate or maintain ILC3s (Fig. S2 B). However, reconstitution was not abolished, indicating that intrinsic impairment alone does not fully account for the phenotype. Conversely, WT donor cells only partially restored ILC3

numbers in *Lingo4*$^{-/-}$ recipients and did not reach WT→WT levels. This incomplete rescue suggests the presence of an additional extrinsic barrier in *Lingo4*$^{-/-}$ hosts, most likely arising from microbiota perturbations, which are known to be further altered by irradiation during chimera generation. These results indicate that the ILC3 numerical defect reflects a combination of intrinsic impairment and microbiota-dependent extrinsic influences. In contrast, IL-22 production mapped entirely to donor genotype: *Lingo4*$^{-/-}$ ILC3s failed to produce IL-22, whereas WT ILC3s produced normal IL-22 regardless of recipient genotype (Fig. S2 C). Together, these findings reveal a dual mechanism, in which ILC3 numbers depend on both intrinsic LINGO4 function and microbiota-derived cues, whereas IL-22 production is exclusively cell intrinsic.

Consistent with a microbiota-dependent component to the numerical phenotype, vancomycin, neomycin, ampicillin, and metronidazole (VNAM) antibiotic treatment abolished differences in ILC3 frequencies between WT and *Lingo4*$^{-/-}$ mice (Fig. 2 C). Under these conditions, IL-22 levels at steady state normalized, but the IL-23–induced IL-22 defect persisted in *Lingo4*$^{-/-}$ cells (Fig. 2 D), reinforcing its intrinsic nature. IL-17 responses showed intermediate sensitivity to microbiota manipulation (Fig. 2 D). Developmental analyses supported this interpretation: before weaning, when the microbiota is immature, ILC3 numbers were similar in WT and *Lingo4*$^{-/-}$ mice (Fig. 2, E and F). After weaning, when microbiota-derived cues intensify, ILC3 numbers declined sharply in *Lingo4*$^{-/-}$ mice. In contrast, IL-22 production was already impaired at birth and remained defective throughout development (Fig. 2 G), confirming a microbiota-independent regulation. IL-17 production showed nonuniform developmental patterns (Fig. S2 D), consistent with partial microbiota sensitivity.

Lingo4 deficiency induces a dysbiotic microbiota with reduced capacity to support ILC3s

To characterize microbial alterations associated with *Lingo4* deficiency, we profiled fecal bacterial communities in cohoused and non-cohoused WT and *Lingo4*$^{-/-}$ mice using 16S rRNA sequencing. α diversity was unchanged (Fig. S2 E), but β diversity revealed distinct clustering of non-cohoused WT and *Lingo4*$^{-/-}$ microbiotas, whereas cohoused mice of both genotypes clustered together (Fig. 2 H and Fig. S2 F). Taxonomic analysis showed that non-cohoused *Lingo4*$^{-/-}$ mice harbored a microbiota markedly different from WT, whereas *Lingo4*$^{-/-}$ mice cohoused with WT mice resembled WT controls (Fig. 2 I and Fig. S2 G). Linear discriminant analysis effect size (LEfSe) confirmed widespread taxonomic differences between genotypes under non-cohoused conditions (Fig. S2, H and I). Cohousing drove extensive restructuring of the *Lingo4*$^{-/-}$ microbiota (Fig. S2 J), but WT microbiota remained stable (Fig. S2 K), revealing asymmetric microbial transfer from WT → *Lingo4*$^{-/-}$ mice. Key differences in non-cohoused *Lingo4*$^{-/-}$ mice included loss of SCFA-producing families (Muribaculaceae and Firmicutes) and expansion of dysbiosis-associated taxa (Tannerellaceae, Helicobacteraceae, and Rhodospirillales) (Fig. S2, H and K).

Phylogenetic investigation of communities by reconstruction of unobserved states (PICRUSt2) functional inference showed that WT microbiota was enriched for SCFA-related metabolic pathways, while *Lingo4*$^{-/-}$ microbiota favored nitrogenous waste metabolism and menaquinone/quinone biosynthesis, features characteristic of inflamed or dysbiotic ecosystems (Fig. S3 A). Because the microbiota of *Lingo4*$^{-/-}$ mice exhibited major shifts in metabolic potential, particularly in pathways linked to fermentation of complex carbohydrates and SCFA production, and because such diet-derived metabolites are known regulators of ILC3 homeostasis (Chun et al., 2019; Fachi et al., 2020), we asked whether dietary inputs would differentially modulate ILC3 abundance in WT and *Lingo4*$^{-/-}$ mice. Dietary manipulation revealed that ILC3 abundance is sensitive to microbiota-driven metabolic cues in both genotypes, but with distinct magnitude effects. A high-fat diet reduced ILC3 numbers in WT mice and further exacerbated the deficit in *Lingo4*$^{-/-}$ mice relative to mice maintained on conventional chow, consistent with diet-induced dysbiosis (Fig. S3 B). Conversely, a high-fiber diet significantly increased ILC3 numbers in WT mice, whereas only a modest trend was observed in *Lingo4*$^{-/-}$ mice (Fig. S3 C), suggesting that fiber supplementation cannot fully overcome the underlying dysbiotic state in the *Lingo4*$^{-/-}$ mice. Under low-fiber conditions, both WT and *Lingo4*$^{-/-}$ mice exhibited similarly reduced ILC3 numbers, consistent with impaired microbial metabolic support in both groups. Together, these findings indicate that *Lingo4* deficiency creates a microbial and metabolic environment less capable of sustaining ILC3 homeostasis, and that diet interacts with this altered microbial landscape in a genotype-dependent manner, providing functional support for the conclusion that microbial metabolic capacity contributes to the ILC3 phenotype.

WT microbiota restores ILC3 numbers in *Lingo4*$^{-/-}$ mice but fails to rescue intrinsic IL-22 defects

Because both the composition and metabolic potential of the *Lingo4*$^{-/-}$ microbiota were altered and because ILC3 numbers showed microbiota dependence, we next asked whether the *Lingo4*$^{-/-}$ microbial community is sufficient to transfer the ILC3 phenotype and whether restoring a WT microbiota can rescue it. To directly test this, we performed fecal microbiota transplantation (FMT) between WT and *Lingo4*$^{-/-}$ mice (Fig. 3 A). Recipients were pretreated with a VNAM antibiotic cocktail for 4 wk to deplete endogenous microbiota and were analyzed 21 days after FMT to allow microbial reconstitution (Fig. 3 B). Transfer of WT microbiota normalized ILC3 numbers in both WT and *Lingo4*$^{-/-}$ recipients (Fig. 3 C), demonstrating that a WT microbial community is sufficient to restore ILC3 abundance even in a *Lingo4*-deficient host. In contrast, transfer of *Lingo4*$^{-/-}$ microbiota reduced ILC3 numbers in both genotypes (Fig. 3 C), establishing that the dysbiotic *Lingo4*$^{-/-}$ microbiota is sufficient to drive the ILC3 numerical defect. Cytokine production displayed distinct dependencies on genotype versus baseline microbiota composition. Although exposure to WT microbiota modestly increased IL-22 and IL-17 production by *Lingo4*$^{-/-}$ ILC3s (WT→KO) compared with *Lingo4*$^{-/-}$ mice that received *Lingo4*$^{-/-}$ microbiota (KO→KO) (Fig. 3, D and E), genotype remained the dominant determinant of cytokine output. *Lingo4*$^{-/-}$ mice maintained lower IL-22 and IL-17 levels than WT mice even after receiving WT microbiota, as shown by comparing WT→KO with WT→WT.

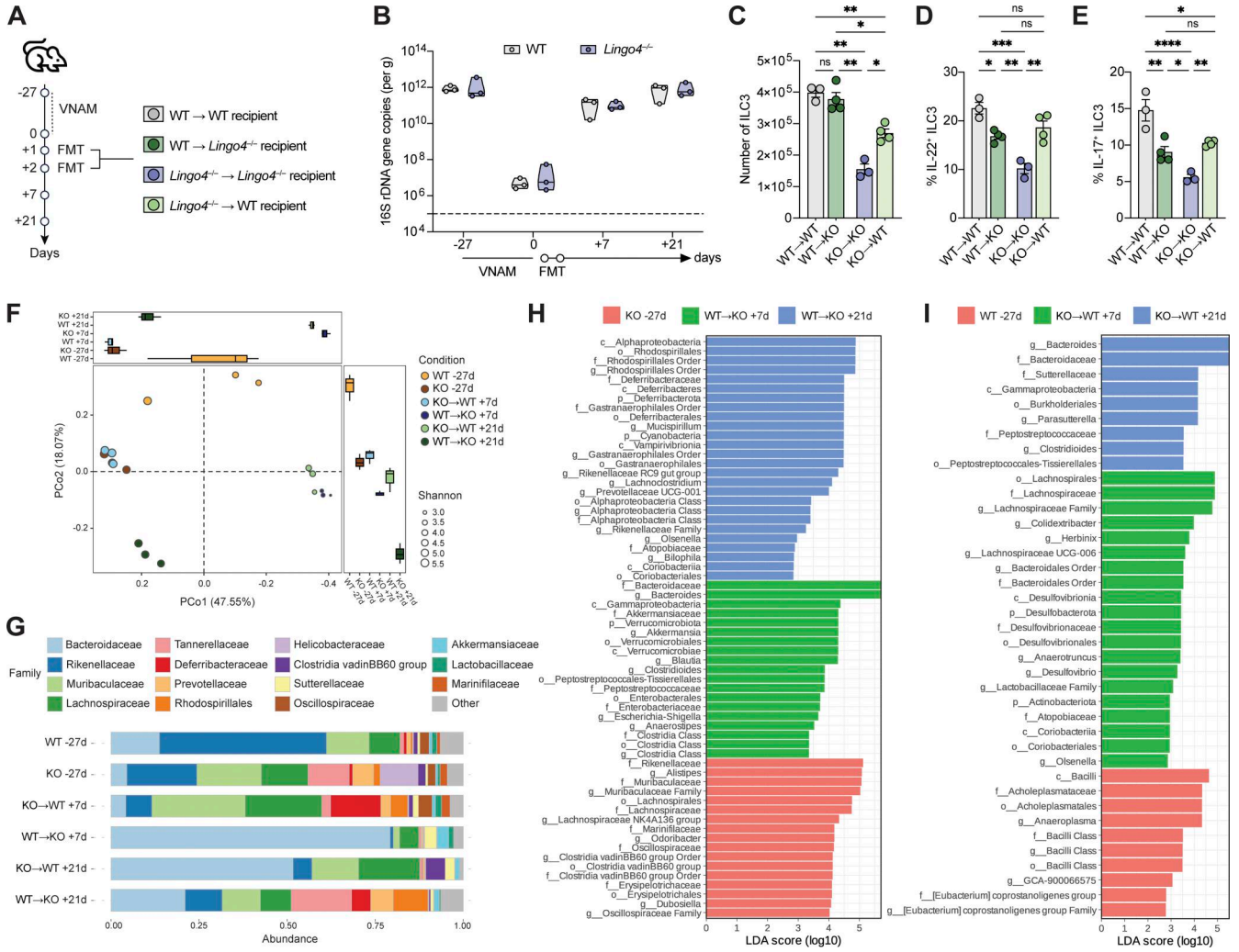

Figure 3. **Microbiota transplantation partially rescues the *Lingo4*$^{-/-}$ ILC3 phenotype. (A and B)** VNAM pretreatment and FMT scheme (A) and total bacterial load measured by 16S rRNA gene copies across the FMT course (B). *n* = 3. **(C–E)** Frequencies of total ILC3s (C), IL-22^{+} ILC3s (D), and IL-17^{+} ILC3s (E) in siLP of WT and *Lingo4*$^{-/-}$ mice after 3 wk of FMT. Mean ± SEM, *n* = 3–4. **(F and G)** Bray–Curtis PCoA (F) and family-level fecal microbiota composition (G) of mice from A. *n* = 4. "WT" refers to wild-type mice and "KO" refers to *Lingo4*$^{-/-}$ mice. **(H and I)** Differentially enriched taxa in *Lingo4*$^{-/-}$ (H) and WT (I) mice by LEfSe. *n* = 4. **(A–E)** Statistical significance was assessed using unpaired two-tailed *t* tests or one-way ANOVA with Tukey's post hoc test. *P < 0.05; **P < 0.01; ***P < 0.001; ****P < 0.0001. PCoA, principal coordinates analysis.

Similarly, IL-22 production by WT ILC3s was not impaired by the *Lingo4*$^{-/-}$ microbiota, as shown by comparing KO→WT and KO→KO or WT→WT and KO→WT (Fig. 3 D). Although IL-17 production was reduced in WT ILC3s following transfer of *Lingo4*$^{-/-}$ microbiota (KO→WT vs. WT→WT), WT ILC3s still produced higher levels of IL-17 than *Lingo4*$^{-/-}$ ILC3s in the same microbial context (KO→WT vs. KO→KO). Together, these findings indicate that the IL-22 defect is primarily cell intrinsic and can be minimally rescued by restoring a normal microbial environment, and the IL-17 defect is partial and context-dependent rather than absolute.

Microbiota profiling revealed genotype-dependent colonization dynamics after FMT. WT recipients rapidly acquired the *Lingo4*$^{-/-}$ microbiota by day 7, but this profile was not maintained by day 21, suggesting that the WT gut environment gradually outcompetes dysbiotic taxa (Fig. 3 F and Fig. S3 D). In contrast, *Lingo4*$^{-/-}$ recipients failed to engraft WT microbiota at day 7 but successfully acquired it by day 21, indicating delayed colonization likely linked to reduced IL-22–dependent barrier function. These dynamics were reflected at the family and genus levels (Fig. 3 G and Fig. S3 E). Across all time points, *Lingo4*$^{-/-}$ mice exhibited persistent expansion of Proteobacteria, a phylum associated with dysbiosis and barrier dysfunction, and reduced Firmicutes, trends supported by Multivariate Association with Linear Models 2 (MaAsLin2) analysis (Fig. S3, F–H). LEfSe further showed that *Lingo4*$^{-/-}$ recipients acquired a broader and more dysbiosis-associated set of taxa than WT recipients: at day 7, *Lingo4*$^{-/-}$ mice were enriched for Bacteroidaceae, Akkermansia, and Verrucomicrobia, and by day 21, they expanded Alphaproteobacteria and Rhodospirillales, whereas WT recipients showed enrichment of Lachnospiraceae and Bacteroidales early and Bacteroides and Gammaproteobacteria later, patterns more consistent with microbiota stabilization than persistent dysbiosis (Fig. 3 H). Together, these results demonstrate that the *Lingo4*$^{-/-}$ microbiota is necessary and sufficient to reduce ILC3

abundance, explaining the extrinsic component of the ILC3 numerical phenotype, whereas IL-22 production remains mainly cell intrinsic and unaffected by microbiota normalization, and that *Lingo4* deficiency alters the host environment in ways that delay microbial engraftment and favor expansion of dysbiosis-associated taxa following FMT.

Lingo4 deficiency impairs microbiota-driven protection against *C. difficile* and *C. rodentium* infections

ILC3-derived IL-22 is a key mediator of epithelial defense and protection against intestinal pathogens (Jarade et al., 2022; Sonnenberg et al., 2011; Cella et al., 2009; Sanos et al., 2009; Satoh-Takayama et al., 2008). Because *Lingo4*$^{-/-}$ mice exhibit a pronounced, cell-intrinsic defect in IL-22 production and a microbiota-dependent reduction in ILC3 numbers, we next examined whether these impairments increase susceptibility to enteric infection. As an initial model of microbiota-dependent infection, we used *C. difficile*, an anaerobic, spore-forming pathogen that requires disruption of the gut microbiota for efficient colonization and causes toxin-mediated colitis (Abt et al., 2016). Following standard antibiotic conditioning (Chen et al., 2008), WT and *Lingo4*$^{-/-}$ mice developed comparable disease during the early phase of infection; however, *Lingo4*$^{-/-}$ mice exhibited significantly increased disease severity at later stages, as shown by greater weight loss and clinical scores on days 4 and 5 p.i. (Fig. S4, A–C). In contrast, when infection was performed without antibiotic pretreatment, thereby preserving microbiota-mediated colonization resistance, WT mice displayed minimal disease, whereas *Lingo4*$^{-/-}$ mice were highly susceptible and developed marked pathology (Fig. S4, D–F). These findings indicate that *Lingo4* deficiency compromises microbiota-driven colonization resistance to *C. difficile*.

To assess whether LINGO4 also regulates susceptibility to microbiota-independent infection, we challenged both cohoused and separately housed WT and *Lingo4*$^{-/-}$ mice with *C. rodentium*, a mucosal pathogen and the murine equivalent of human enterohemorrhagic *Escherichia coli* (Collins et al., 2014). Non-cohoused *Lingo4*$^{-/-}$ mice showed the greatest susceptibility, with more severe body weight loss, elevated early fecal bacterial burdens, and delayed pathogen clearance relative to WT mice (Fig. 4, A and B). These mice also exhibited classic signs of mucosal injury, including shortened colon length (Fig. 4 C), increased fecal lipocalin-2 (Fig. 4 D), and enhanced gut permeability measured by serum fluorescein isothiocyanate (FITC-dextran) (Fig. 4 E). Histopathology confirmed more extensive tissue damage in both small intestine and colon (Fig. 4 F), accompanied by increased colonic myeloid infiltration (Fig. 4 G). In parallel, non-cohoused *Lingo4*$^{-/-}$ mice showed marked reductions in ILC3 numbers and diminished production of IL-22, IL-17, and IFN-γ in small intestine (Fig. 4, H and I) as well as in colon (Fig. 4, J and K), consistent with a failure to mount effective mucosal immune responses. Notably, cohousing *Lingo4*$^{-/-}$ with WT mice partially mitigated disease severity, reducing weight loss and bacterial burden relative to non-cohoused *Lingo4*$^{-/-}$ mice (Fig. 4, A and B), consistent with microbiota-mediated rescue of ILC3 abundance.

To directly test whether IL-22 deficiency is responsible for the increased susceptibility of *Lingo4*$^{-/-}$ mice, we manipulated IL-22 signaling during *C. rodentium* infection (Fig. 4 L). IL-22 blockade in WT mice eliminated their natural resistance, producing a disease course that phenocopied non-cohoused *Lingo4*$^{-/-}$ mice and further increasing susceptibility in *Lingo4*$^{-/-}$ mice (Fig. 4, M and N). Conversely, treatment with recombinant IL-22 fully restored resistance to *C. rodentium* in *Lingo4*$^{-/-}$ mice to levels comparable with WT controls. These findings demonstrate that impaired IL-22–dependent mucosal immunity is a major driver of the heightened susceptibility of *Lingo4*$^{-/-}$ mice and that restoring IL-22 is sufficient to reverse this defect.

Finally, because *Lingo4* transcript is also expressed in select T cell subsets (Fig. S1, C–I), we tested whether aberrant T cell function contributes to the infection phenotype, given prior evidence implicating T cells in the regulation of host responses (Zindl et al., 2024). *Lingo4*$^{-/-}$ mice crossed to *Rag1*$^{-/-}$, *Tcrb*$^{-/-}$, or *Tcrd*$^{-/-}$ backgrounds remained highly susceptible to *C. rodentium* infection compared with their *Lingo4*$^{+/+}$ counterparts (Fig. S4, G–N), demonstrating that the increased susceptibility of *Lingo4*$^{-/-}$ mice is independent of αβ and γδ T cells. Together, these results show that *Lingo4* deficiency compromises both microbiota-mediated protection and IL-22–driven mucosal immunity, leading to heightened vulnerability to intestinal pathogens; cohousing with WT mice and IL-22 supplementation each partially correct distinct components of this defect.

Lingo4 deficiency protects against *S. typhimurium* by limiting IL-22

Because IL-22 can play a detrimental role during *S. typhimurium* infection by inducing antimicrobial programs that suppress protective commensal competitors but spare *S. typhimurium*, thereby promoting pathogen expansion (Behnsen et al., 2014; Xiong et al., 2022), we reasoned that the intrinsic IL-22 defect in *Lingo4*$^{-/-}$ mice might confer relative protection to this pathogen. Consistent with this hypothesis, non-cohoused *Lingo4*$^{-/-}$ mice were significantly more resistant to *S. typhimurium* challenge than WT controls, exhibiting improved survival, reduced body weight loss, lower fecal bacterial burdens (Fig. 5, A–C), and decreased bacterial dissemination to mesenteric LNs and liver (Fig. S5, A–D). *Lingo4*$^{-/-}$ mice also showed reduced colon shortening (Fig. S5 E), lower histopathological scores in both small intestine and colon (Fig. 5, D and E), increased goblet cell numbers (Fig. 5 F), and reduced infiltration of neutrophils and inflammatory monocytes (Fig. 5 G), indicating enhanced barrier integrity and attenuated inflammation. Importantly, streptomycin pretreatment, which is commonly used to facilitate infection in WT mice by inducing dysbiosis (Walker et al., 2023), abolished the enhanced resistance of *Lingo4*$^{-/-}$ mice, indicating that their protection depends on an intact commensal microbiota and is lost when the microbiota is disrupted.

To identify the mechanism underlying this enhanced resistance, we assessed ILC3 responses and found that ILC3 frequencies and IL-22 production were markedly reduced in *Lingo4*$^{-/-}$ mice on day 5 p.i. (Fig. 5, H and I), consistent with diminished IL-22–driven suppression of commensals. To directly test the role of IL-22, we manipulated IL-22 signaling during infection. Neutralization of IL-22 increased survival of WT mice, rendering them phenotypically similar to *Lingo4*$^{-/-}$

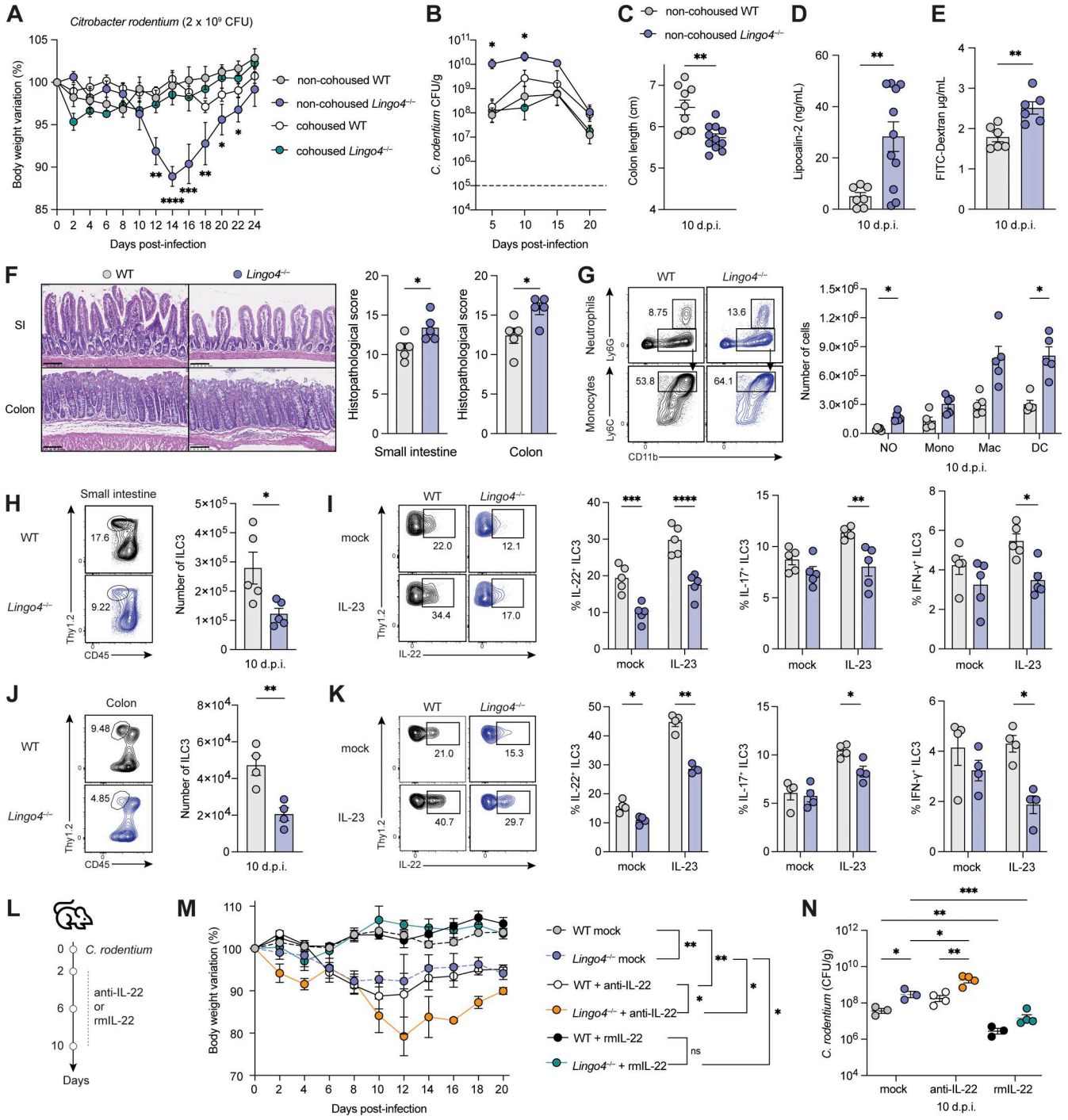

Figure 4. ***Lingo4*$^{-/-}$ mice are more susceptible to *C. rodentium* infection due to impaired IL-22–mediated mucosal protection.** **(A)** Body weight variation in cohoused and non-cohoused WT and *Lingo4*$^{-/-}$ mice during *C. rodentium* infection. Mean ± SEM, *n* = 15; three experiments combined. **(B)** Fecal *C. rodentium* burden at 5, 10, 15, and 20 d.p.i. Mean ± SEM, *n* = 9–11; two experiments combined. **(C–E)** Colon length (C), fecal lipocalin-2 levels (D), and intestinal permeability by FITC-dextran (E) at 10 d.p.i. Mean ± SEM, *n* = 9–11 (C–D) and *n* = 5 (E). **(F)** Representative H&E sections of colon and small intestine with histopathological scoring at 10 d.p.i. Mean ± SEM, *n* = 5. Scale bars = 100 µm. **(G)** Representative plots and absolute numbers of myeloid cells in colon at 10 d.p.i. Mean ± SEM, *n* = 5; representative of two experiments. "NO," neutrophils; "Mono," monocytes; "Mac," macrophages; "DC," dendritic cells. **(H and I)** Representative plots and absolute numbers of siLP ILC3s (H) and IL-22^{+}, IL-17^{+}, and IFN-γ^{+} siLP ILC3 (I) frequencies after *ex vivo* IL-23 stimulation at 10 d.p.i. Mean ± SEM, *n* = 5; representative of two experiments. ILC3s were defined as live lymphocyte-sized Lin^{-} (CD3^{-} CD19^{-}) Thy1.2^{hi} CD45^{int} cells. **(J and K)** Representative plots and absolute numbers of colonic ILC3s (J) and IL-22^{+}, IL-17^{+}, and IFN-γ^{+} colonic ILC3 (K) frequencies after *ex vivo* IL-23 stimulation at 10 d.p.i. Mean ± SEM, *n* = 5; representative of two experiments. ILC3s were defined as live lymphocyte-sized Lin^{-} (CD3^{-} CD19^{-}) Thy1.2^{hi} CD45^{int} cells. **(L–N)** Schematic of IL-22 neutralization or recombinant IL-22 (rmIL-22) therapy during infection (L), relative body weight (M), and fecal *C. rodentium* burden at 10 d.p.i. (N). Mean ± SEM, *n* = 4. **(A–N)** Statistical significance was determined using unpaired two-tailed *t* test or one-way ANOVA with Tukey's post hoc test. *P < 0.05; **P < 0.01; ***P < 0.001; ****P < 0.0001.

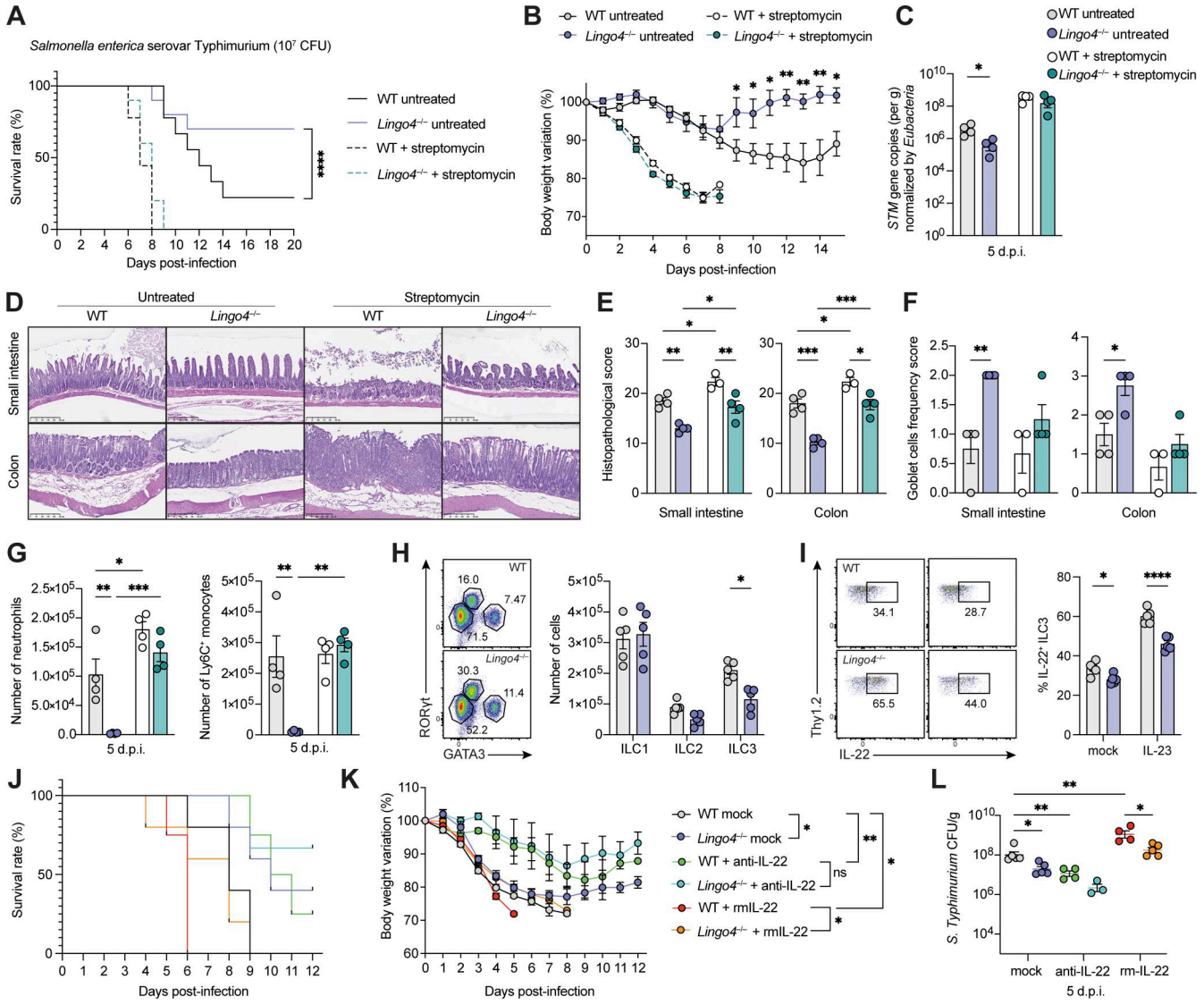

Figure 5. ***Lingo4*$^{-/-}$ mice are more resistant to *S. typhimurium* infection due to reduced IL-22–mediated pathology. (A and B)** Survival (A) and body weight change (B) of WT and *Lingo4*$^{-/-}$ mice infected with *S. typhimurium*, with or without streptomycin pretreatment. *n* = 18–20; three experiments combined. **(C)** Fecal *S. typhimurium* burden at 5 d.p.i., normalized to total Eubacteria 16S rRNA gene copies. Mean ± SEM, *n* = 4; representative of two experiments. **(D–F)** Representative H&E sections (D), histopathological score (E), and goblet cell frequency (F) at 5 d.p.i. Mean ± SEM, *n* = 4. Scale bars = 100 µm. **(G and H)** Numbers of neutrophils and inflammatory monocytes (G) and ILC3s (H) in siLP at 5 d.p.i. Mean ± SEM, *n* = 4–5; representative of two experiments. **(I)** Frequencies of IL-22$^+$ ILC3s after IL-23 stimulation at 5 d.p.i. Mean ± SEM, *n* = 5. **(J–L)** Survival (J), body weight (K), and fecal *S. typhimurium* burden (L) in WT and *Lingo4*$^{-/-}$ mice treated with anti–IL-22 or rmIL-22 on days 0, 2, and 4 p.i. Mean ± SEM, *n* = 4. **(A–L)** Statistical significance was determined using unpaired two-tailed *t* test or one-way ANOVA with Tukey's post hoc test. *P < 0.05; **P < 0.01; ***P < 0.001; ****P < 0.0001. rmIL-22, recombinant IL-22.

mice, whereas administration of recombinant IL-22 eliminated protection in *Lingo4*$^{-/-}$ mice and further worsened outcomes in WT mice (Fig. 5, J–L). These experiments demonstrate that reduced IL-22 production is the key driver of the enhanced resistance of *Lingo4*$^{-/-}$ mice to *S. typhimurium* by limiting pathogen-favoring suppression of the microbiota.

Because *Lingo4* transcript is expressed in select T cell subsets and conventional CD4$^+$ T cells contribute to late-stage pathogen control (Pedicord et al., 2016; van der Velden et al., 2005; Clay et al., 2020), we examined whether T cells participate in this phenotype. Although CD4$^+$ T cell numbers were modestly reduced in *Lingo4*$^{-/-}$ mice at day 5 p.i. (Fig. S5 F), the protective phenotype persisted when WT and *Lingo4*$^{-/-}$ mice were compared on a *Rag1*$^{-/-}$ background but was lost following streptomycin pretreatment (Fig. S5, G and H). These results indicate that the enhanced resistance of *Lingo4*$^{-/-}$ mice is driven primarily by reduced ILC3 abundance and diminished IL-22 production, rather than by alterations in conventional T cell compartments.

LINGO4 controls ILC3 activation through mitochondrial regulation

To investigate the mechanistic basis of LINGO4 function, we generated a LINGO4-overexpressing 293T cell line in which an N-terminal FLAG tag and a C-terminal 6xHis tag were fused to

LINGO4 (Fig. 6 A). Flow cytometry and anti-FLAG immunofluorescence revealed that LINGO4 is expressed predominantly intracellularly, with lower surface expression (Fig. 6, A and B). Immunoprecipitation of LINGO4 with anti-FLAG antibody followed by mass spectrometry identified proteins enriched in LINGO4-expressing cells but not control 293T cells (Table S1), and pathway analysis of these interactors revealed strong associations with mitochondrial and ER processes, including mitochondrial membrane transport, calcium trafficking, and protein folding (Fig. 6 C). Notably, bulk RNA sequencing of sort-purified ILC3s from *Lingo4*$^{-/-}$ and WT mice revealed a similar enrichment of pathways linked to mitochondrial function and ER protein processing (Fig. 6 D), suggesting that LINGO4 regulates fundamental metabolic and organelle-associated processes in ILC3s.

Given that mitochondrial metabolism is essential for ILC3 activation, proliferation, and cytokine production, including IL-22 and IL-17 (Di Luccia et al., 2019; Yu et al., 2022), we examined mitochondrial structure and function in *Lingo4*-deficient ILC3s. Electron microscopy of sort purified siLP ILC3s showed that *Lingo4*$^{-/-}$ ILC3s have reduced mitochondrial matrix density, indicative of structural abnormalities (Fig. 6 E). MitoTracker Green staining of WT and *Lingo4*$^{-/-}$ ILC3s revealed no difference in mitochondrial mass at steady state or following IL-23 stimulation, and baseline mitochondrial membrane potential shown by MitoTracker Red staining was comparable between genotypes (Fig. 6 F). However, upon IL-23 stimulation, WT ILC3s increased their mitochondrial membrane potential, whereas *Lingo4*$^{-/-}$ ILC3s failed to undergo this metabolic activation (Fig. 6 F), demonstrating an impaired ability to engage mitochondrial respiration during activation.

We next assessed mitochondrial ROS (mROS) by mitoSOX staining. *Lingo4*$^{-/-}$ ILC3s produced significantly more mROS than WT ILC3s (Fig. 6 G), consistent with metabolic stress. Because excessive mROS promotes lipid peroxidation, we quantified oxidized lipids using BODIPY 581/591 C11. *Lingo4*$^{-/-}$ ILC3s displayed elevated lipid accumulation and lipid peroxidation (Fig. 6 H), indicating impaired cellular metabolism and oxidative damage to mitochondrial membranes. STAT3 activation integrates cytokine signaling with mitochondrial metabolic programming in ILC3s (Lehmann et al., 2020; Guo et al., 2014; Teufel et al., 2021). Although *Lingo4* deficiency did not impair RORγt expression (Fig. 1 F), *Lingo4*$^{-/-}$ ILC3s exhibited reduced phosphorylation of STAT3 following IL-23 stimulation (Fig. 6 I). These data suggest that defective STAT3 activation, together with mitochondrial dysfunction, underlies the impaired IL-22 production observed in *Lingo4*$^{-/-}$ ILC3s. Because lipid peroxidation and mitochondrial damage can trigger apoptosis, we assessed cell survival. Annexin V staining revealed that *Lingo4*$^{-/-}$ ILC3s contained more early apoptotic cells and fewer viable cells than WT ILC3s (Fig. 6 J), whereas Ki67 staining showed normal proliferative capacity (Fig. 6 K). These results suggest that reduced ILC3 abundance in *Lingo4*$^{-/-}$ mice arises primarily from increased susceptibility to apoptosis rather than impaired proliferation.

Finally, to confirm that the impaired mitochondrial phenotype is intrinsic to ILC3s, we analyzed *Lingo4*$^{\Delta ILC3}$ mice. Compared with *Lingo4*$^{fl/fl}$ controls, ILC3s from *Lingo4*$^{\Delta ILC3}$ mice exhibited significantly increased mitochondrial ROS (Fig. 7 A), elevated lipid peroxidation (Fig. 7 B), reduced STAT3 phosphorylation (Fig. 7 C), and enhanced apoptosis (Fig. 7 D). Consistent with these cellular defects, *Lingo4*$^{\Delta ILC3}$ mice were more susceptible to *C. rodentium* infection, as reflected by greater body weight loss (Fig. 7 E) and higher fecal bacterial burden (Fig. 7 F). Moreover, *Lingo4*$^{\Delta ILC3}$ mice showed a marked reduction in colonic ILC3 numbers and diminished production of IL-22 and IL-17, but not IFN-γ, TNF-α, or GM-CSF (Fig. 7, G–I), consistent with the phenotype observed in *Lingo4*$^{-/-}$ mice (Fig. 4).

Together, these findings indicate that LINGO4 sustains ILC3 survival and effector function by preserving mitochondrial fitness, limiting mROS, maintaining STAT3 activation, and preventing apoptosis. Loss of LINGO4 impairs IL-22 production intrinsically, compromising epithelial barrier integrity and promoting dysbiosis. Consistent with prior studies showing that reduced IL-22 drives transmissible dysbiosis (Zenewicz et al., 2013), whereas enhanced IL-22 signaling promotes protective microbial communities (Fachi et al., 2024), the microbiota alterations in *Lingo4*$^{-/-}$ mice reflect diminished IL-22 output. The resulting dysbiotic environment further restricts ILC3 maintenance, establishing a dual mechanism: a primary cell-intrinsic metabolic defect and a secondary microbiota-dependent amplification of ILC3 loss.

Discussion

This study identifies LINGO4 as a previously unrecognized, dual regulator of ILC3 biology that couples cell-intrinsic effector programs to microbiota-dependent homeostasis. Members of the LINGO family (LINGO1–4) share conserved structural features, including leucine-rich repeats and immunoglobulin-like domains, and have been primarily studied in the context of neuronal signaling (Guillemain et al., 2020). LINGO1 has been extensively characterized in the nervous system, where it functions as a regulatory subunit of large-conductance Ca^{2+}-activated potassium channels and has been implicated in tremor and neurodegenerative disorders (Dudem et al., 2020; Mi et al., 2007; Inoue et al., 2007). LINGO2 and LINGO3 have emerged as modulators of intestinal epithelial biology, acting as components of receptor complexes for trefoil factors that regulate EGFR signaling, mucosal wound healing, stem cell maintenance, and host defense during colitis and helminth infection (Belle et al., 2019; Zullo et al., 2021). Despite these advances, LINGO4 has remained largely unexplored, with prior studies primarily linking its expression to embryonic neuronal development and no established role in immune regulation (Haines and Rigby, 2008; Guillemain et al., 2020). Here, we demonstrate that LINGO4 is highly expressed in RORγt$^+$ ILC3s and is intrinsically required for their metabolic fitness, STAT3 activation, IL-22 production, and survival. By extending the functional repertoire of the LINGO family beyond neuronal and epithelial compartments, these findings uncover LINGO4 as a regulator that fine-tunes ILC3 function and IL-22–dependent intestinal barrier immunity.

Our work advances the ILC3 field in several important ways. First, it uncouples ILC3 numbers from effector function by demonstrating that LINGO4 plays a strongly cell-intrinsic role in

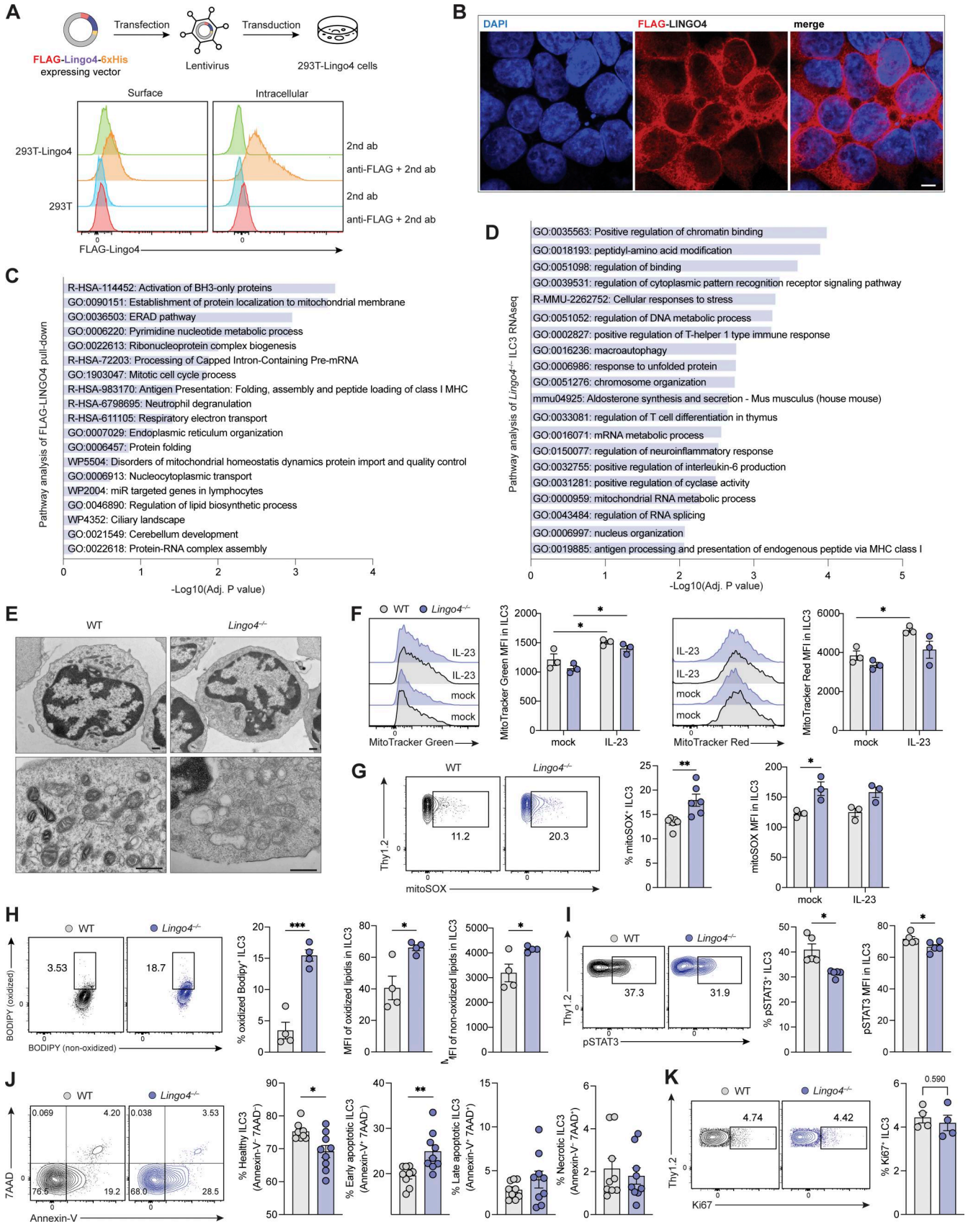

Figure 6. ***Lingo4* is required to sustain mitochondrial function in ILC3s. (A)** Scheme: 293T cell were stably transfected with *Lingo4* having FLAG-tag was fused to its N-terminal part and 6xHis-tag to its C-terminal part. Flow cytometry histograms of surface and intracellular LINGO4 expression on 293T cells by

anti-FLAG staining. Representative of three experiments. **(B)** Representative immunofluorescence image of FLAG-positive 293T-Lingo4 cells. Scale bar: 5 µm. Representative of three experiments. **(C)** Pathway analysis of proteins immunoprecipitated with anti-FLAG antibody from 293T-Lingo4 cells but not from 293T control cells (n = 100; peptide coverage ≥10%). **(D)** Pathway analysis of DEGs obtained by RNA-seq analysis of sort purified siLP ILC3 from WT and *Lingo4*$^{-/-}$ mice. n = 4; padj < 0.01. **(E)** Representative TEM images of sort purified siLP ILC3 from WT and *Lingo4*$^{-/-}$ mice. n = 4. Scale bars, 500 nm. **(F)** Representative flow cytometry plots and MFI of MitoTracker Green and MitoTracker Red staining in WT and *Lingo4*$^{-/-}$ siLP ILC3 upon *ex vivo* stimulation. Mean ± SEM, n = 3; representative of two experiments. **(G)** Representative flow cytometry plots and frequency of mitoSOX^{+} siLP ILC3s from WT and *Lingo4*$^{-/-}$ mice. Mean ± SEM, n = 6; two experiments combined. **(H)** Representative flow cytometry plots, frequency, and MFI of lipids staining by BODIPY 581/591 C11 in WT and *Lingo4*$^{-/-}$ siLP ILC3s. Mean ± SEM, n = 4; representative of two experiments. **(I)** Representative flow cytometry plots, frequency, and MFI of pSTAT3^{+} siLP ILC3. Mean ± SEM, n = 5; representative of two experiments. **(J)** Representative flow cytometry plots and frequency of Annexin-V and 7AAD staining of siLP ILC3. Mean ± SEM, n = 9; three experiments combined. **(K)** Representative flow cytometry plots and frequency of Ki67 staining siLP ILC3. Mean ± SEM, n = 4; representative of two experiments. **(F–K)** Statistical significance was determined using unpaired two-tailed t test or one-way ANOVA with Tukey's post hoc test. *P < 0.05; **P < 0.01; ***P < 0.001.

regulating IL-22 production, while contributing only modestly and indirectly to ILC3 numbers. ILC3s serve as key sentinels of the intestinal barrier, producing IL-22 to promote epithelial defense, shape commensal microbial communities, and restrict pathogen expansion (Horn and Sonnenberg, 2024), yet the mechanisms that separately govern their functional output versus population size have remained poorly defined. Using mixed bone marrow chimeras and ILC3-specific deletion, we show that the defect in IL-22 production is strictly intrinsic to *Lingo4*-deficient ILC3s. In contrast, co-housing, antibiotic treatment, developmental timing, dietary interventions, and FMT collectively demonstrate that reduced ILC3 abundance arises predominantly from extrinsic, microbiota-dependent cues. Consistent with prior work, microbial composition, microbially derived metabolites, and microbial regulation of IL-23 are well positioned to influence ILC3 survival, activation, and tissue adaptation (Buonocore et al., 2010; Hou et al., 2022; Kabil et al., 2025; Fachi et al., 2020; Chun et al., 2019).

Second, we define a metabolic mechanism downstream of LINGO4 in the context of emerging evidence that mitochondrial fitness is central to ILC3 effector programs. *Lingo4*-deficient ILC3s display abnormal mitochondrial ultrastructure, fail to increase mitochondrial membrane potential upon activation, accumulate mROS and lipid peroxidation products, show reduced STAT3 phosphorylation, and undergo increased apoptosis despite preserved proliferation. Consistent with prior work demonstrating that ILC3s integrate glycolysis with mitochondrial respiration and mROS generation to sustain HIF1α activity, RORγt expression, and IL-22 production (Di Luccia et al., 2019; Pral et al., 2021; Wu et al., 2022; Yu et al., 2022; Fonseca-Pereira et al., 2025), our data indicate that LINGO4 is required to couple mitochondrial dynamics to cytokine output. Together, this places LINGO4 upstream of a mitochondrial-STAT3 axis that is essential for ILC3 activation and IL-22 output, aligning with current models in which metabolic sensors and mitochondrial signaling pathways calibrate tissue-resident ILC3 survival, homeostasis, and barrier-protective function.

A third advance of this study is the identification of LINGO4 as a context-dependent regulator of IL-22 production and ILC3 homeostasis with opposing effects across enteric infections. In *C. difficile* and *C. rodentium* models, where IL-22–mediated epithelial repair and antimicrobial peptide production are protective (Abt et al., 2015; Fachi et al., 2020; Zheng et al., 2008; Zhu et al., 2022), *Lingo4* deficiency compromises microbiota-mediated colonization resistance and IL-22–dependent barrier immunity, resulting in exacerbated disease. In contrast, during *S. typhimurium* infection, where IL-22 can promote pathogen expansion by suppressing protective commensals (Xiong et al., 2022; Behnsen et al., 2014), the intrinsic IL-22 defect in *Lingo4*$^{-/-}$ ILC3s confers a survival advantage by limiting pathogen-favoring dysbiosis. These findings highlight that IL-22 is not uniformly beneficial and position LINGO4 as a molecular rheostat that tunes IL-22 output and ILC3 metabolic fitness to shape host–pathogen interactions. Notably, LINGO4 is located near the human *RORC* locus and is expressed in human RORγt^{+} lymphocyte subsets, suggesting that variation in LINGO4 expression or function may influence susceptibility to ILC3-driven diseases such as inflammatory bowel disease, *C. difficile* colitis, or invasive *Salmonella* spp. infection. Together, these data raise the possibility that targeting LINGO4 or its downstream pathways could enable selective modulation of IL-22 responses, enhancing epithelial protection and microbiota stability in some settings while restraining IL-22–driven pathogen expansion or inflammation in others.

The precise molecular interactors that link LINGO4 to mitochondrial and ER homeostasis remain undefined. Given that mass spectrometry identified protein interactors involved also in ER compartment and protein processing, LINGO4 may function at the interface of mitochondrial metabolism and vesicular trafficking, potentially influencing autophagy–lysosomal pathways. This possibility is supported by parallels with another leucine-rich repeat protein, LRRK2, which connects vesicle dynamics to mitochondrial integrity (Wang et al., 2012; Weindel et al., 2020). It also remains to be determined whether analogous LINGO4-dependent mechanisms operate in human ILC3s or Th17 cells *in vivo*. In parallel, although our microbiome analyses identify major taxonomic and functional shifts in *Lingo4*$^{-/-}$ mice, the specific microbial species and metabolites that support or impair ILC3 homeostasis have yet to be defined. Future studies dissecting LINGO4 signaling complexes, examining human tissues, and functionally testing candidate microbial metabolites will be important for extending these findings to broader principles of RORγt^{+} lymphocyte biology and for informing potential therapeutic strategies in mucosal disease.

Materials and methods

Mice

All the protocols and procedures involving animals were approved by Institutional Animal Care and Use Committee at

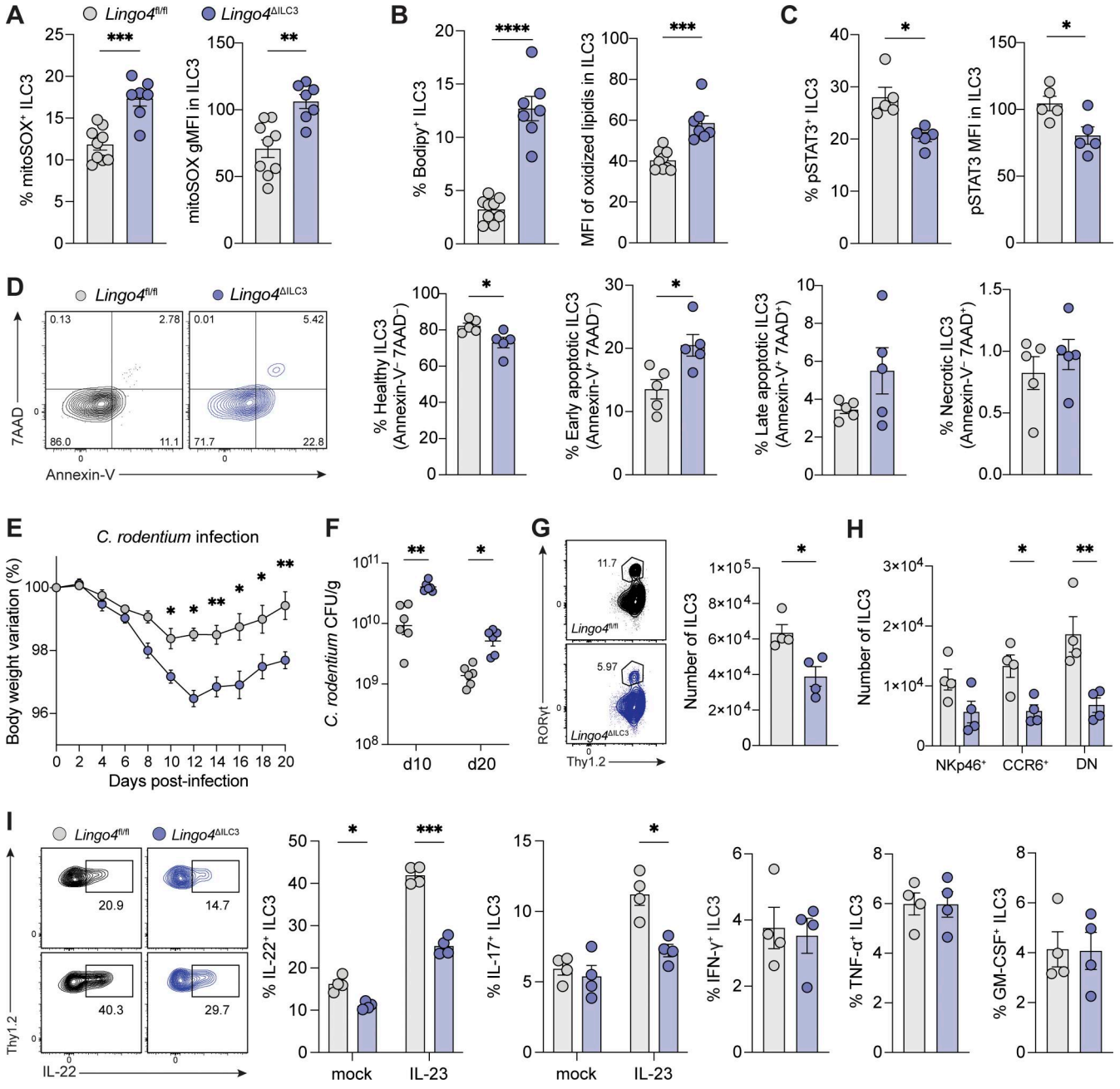

Figure 7. **Impaired ILC3 function is retained in *Lingo4*$^{\Delta ILC3}$ mice. (A)** Frequency and MFI of mitoSOX$^+$ siLP ILC3s from *Lingo4*$^{fl/fl}$ and *Lingo4*$^{\Delta ILC3}$ mice. Mean ± SEM, *n* = 8–9; two experiments combined. **(B)** Frequency of BODIPY 581/591 C11–positive cells and MFI in *Lingo4*$^{fl/fl}$ and *Lingo4*$^{\Delta ILC3}$ siLP ILC3s. Mean ± SEM, *n* = 8–9; two experiments combined. **(C)** Frequency and MFI of pSTAT3$^+$ siLP ILC3. Mean ± SEM, *n* = 5. **(D)** Representative flow cytometry plots and frequency of Annexin-V and 7AAD staining of siLP ILC3. Mean ± SEM, *n* = 5. **(E and F)** Body weight variation (E) and fecal *C. rodentium* burden at 10 and 20 d.p.i. (F) of *Lingo4*$^{fl/fl}$ and *Lingo4*$^{\Delta ILC3}$ mice during *C. rodentium* infection. Mean ± SEM, *n* = 6. **(G–I)** Representative plots and absolute numbers of colonic ILC3s (G), ILC3 subsets (H), and cytokine production by colonic ILC3 at 10 d.p.i. Mean ± SEM, *n* = 4. ILC3s were defined as live lymphocyte-sized Lin$^-$ (CD3$^-$ CD19$^-$) Thy1.2^{hi} CD45^{int} cells. **(A–I)** Statistical significance was determined using unpaired two-tailed *t* test or one-way ANOVA with Tukey's post hoc test. *P < 0.05; **P < 0.01; ***P < 0.001, ****P < 0.0001.

Washington University in St. Louis. All mice were bred and maintained at specific pathogen-free facility at Washington University in St. Louis, MO, USA. C57BL/6J, B6.SJL-*Ptprc*^{a} *Pepc*^{b}/BoyJ (CD45.1), C57BL/6J-*Rag1*^{em10Lutzy}/J (*Rag1*$^{-/-}$), B6.129P2-*Tcrb*^{tm1Mom}/J (*Tcrb*$^{-/-}$), and B6.129P2-*Tcrd*^{tm1Mom}/J (*Tcrd*$^{-/-}$) mice were purchased from Jackson Laboratory. *Serinc2*^{iCre} mice were previously generated by our group (Rodrigues et al., 2025). *Lingo4*$^{-/-}$ and *Lingo4*$^{fl/fl}$ mice were generated at the Washington University School of Medicine in St. Louis. The *Lingo4* allele deletion was generated by CRISPR/Cas9 endonuclease-mediated genome editing. Two guide RNAs (gRNAs) were chosen to include the portion of exon 2 encoding the signal peptide of *Lingo4*: MS872.Lingo4.sp12 (5′-TACTGATGCTCCCTCCAGGCNGG-3′) and MS872.Lingo4.sp6 5′-GTGACTGCACCTCCCAGACCNGG-3′).

gRNAs and a plasmid encoding Cas9 were introduced into C57BL/6J embryos, which were transferred into pseudopregnant females. Several founders were identified by sequencing of the targeted region, and we chose one with a 37 bp insertion created by a 7 bp deletion along with a 44 bp insertion derived from the gRNA scaffold portion of the SpCas9 plasmid. This deletion/insertion disrupted translation/expression of *Lingo4*. For the generation of *Lingo4*$^{fl/fl}$ mice, CRISPR/Cas9 ribonucleoproteins comprising Cas9 protein and gRNAs targeting two regions flanking exon 2 were introduced into C57BL/6J zygotes together with LoxP sites complementary to the targeted regions at 0.5 days after fertilization by electroporation. The edited embryos were then transferred into D0.5 pseudopregnant C57BL/6J recipient females. Confirmed founders were bred to C57BL/6J mice, and the line was maintained as *Lingo4*$^{fl/fl}$ homozygous mice. *Serinc2*^{iCre} were backcrossed to *Lingo4*$^{fl/fl}$ mice (*Lingo4*-$^{\Delta ILC3}$). *Tcrb*$^{-/-}$, *Tcrd*$^{-/-}$, and *Rag1*$^{-/-}$ mice were backcrossed to *Lingo4*$^{-/-}$ mice. Experiments were conducted using sex-matched mice aged 7–14 wk that were either non-cohoused or cohoused from birth. Up to five mice were housed in filtered cages with corn cob bedding, provided with standard chow diet (SD) and drinking water *ad libitum*, and subjected to 12-h light:12-h dark cycles. Cages were cleaned weekly in a laminar airflow cabinet.

Generation of 293T cell line expressing *Lingo4*

Lingo4, flanked by FLAG-tag at N terminus and 6xHis tag at C terminus, was cloned into pLVX-EF1a-IRES-mCherry vector (No. 631987; Clontech Laboratories, Inc.) by Gibson Assembly Cloning Kit (NEB) and confirmed by sequencing. Lentiviral packaging was performed in the 293T packaging cell line (CRL-3216; ATCC) with Lipofectamine 2000 (Thermo Fisher Scientific) as per the manufacturer's protocol. Cells were co-transfected with psPAX2 packaging plasmid (No. 12260; Addgene), pCMV-VSV-G envelope plasmid (No. 8454; Addgene), and pLVX-EF1a-IRES-mCherry expressing FLAG-Lingo4-6xHis. Viral supernatants were harvested 48 h after transfection and passed through 0.45-µm filters. Transduction of 293T cells was conducted in the 12-well plate with 1 ml of filtered viral supernatant supplemented with polybrene (8 µg/ml) and centrifugation at 900 *g* for 1.5 h at RT. The medium was changed next day, and cells were cultured for an additional 5 days. Stably transduced cells were sorted based on mCherry fluorescence using a BD FACS Aria II cell sorter.

Isolation of intraepithelial lymphocytes and LP cells

Small intestine or colon was harvested from mice, cleaned of Payer's patches and/or luminal content, and opened lengthwise. Intraepithelial lymphocytes (IELs) were isolated by incubating the tissue in HBSS with HEPES, 10% bovine calf serum, and 5 mM EDTA for 20 min on the rotator, followed by vigorous vortexing and another round of incubation in HBSS and vortexing. DL-Dithiothreitol (MilliporeSigma) at final concentration of 5 mM was added to supernatants for additional 20 min incubation. For LP cells extraction, the tissue was further digested in 10% RPMI medium containing 1 mg/ml collagenase IV (MilliporeSigma) for 40 min with vigorous shaking at 37°C. Both, IEL and LP leukocytes were purified by density gradient centrifugation using a 40 and 70% Percoll (Cytiva) gradient.

Flow cytometry

Single-cell suspensions were incubated in the Fc block (2.4G2) and immunostained with the following anti-mouse antibodies: CD45 (30-F11), CD11b (M1/70), CD11c (N418), F4/80 (BM8), Ly6C (HK1.4), Ly6G, (1A8), I-A/I-E (M5/114.15.2), CD170 (Siglec-F; S17007L), NKp46 (CD335; 29A1.4), IL-17 (TC11-18H10.1), IFN-γ (XMG1.2), TNF-α (MP6-XT22), GM-CSF (MP1-22E9), CD45.1(A20), CD45.2 (104), NK1.1 (PK136), Thy1.2 (CD90.2; 30-H12), CD8 (53–6.7), CD4 (GK1.5), TCR γ/δ (GL3), CD3ε (145-2C11), CD19 (6D5), Foxp3 (MF-14), KLRG1 (2F1/KLRG1) (all BioLegend), CCR6 (CD196; 140706), GATA3 (L50-823), T-bet (04–46), and Ki67 (16A8) (all BD Biosciences); IL-22 (1H8PWSR) and RORgt (AFKJS-9) (both eBio/Thermo Fisher Scientific); anti-FLAG (#200-310-B13; Rockland); and Alexa-Fluor-647 goat anti-mouse IgG (H+L) (A-21236; Invitrogen). Dead cells were excluded using the Zombie Aqua Fixable Viability Kit (BioLegend). Cell counting was performed using counting beads (eBioscience). For intracellular staining, cells were fixed and permeabilized using the Cytofix/Cytoperm Fixation/Permeabilization Kit (BD Biosciences), and for transcription factor staining, the Foxp3/Transcription Factor Staining Buffer Set (BD Biosciences). For cytokine analysis, cells were stimulated with 10 ng/ml IL-23 (Proteintech) for 3 h with addition of GolgiPlug (BD Biosciences). Mitochondria analysis was performed by staining of cells with MitoTracker Green FM (#M7514), MitoTracker Red FM (#M22425), mitoSOX Red mitochondrial superoxide indicator (#M36008), or BODIPY 581/591 C11 (#D3861) for 30 min at 37°C following surface cell staining. pSTAT3-staining was performed with ant-pSTAT3 (pY795; BD Biosciences) antibody in methanol-fixed cells. ILC3 apoptosis was assessed with the BD Pharmingen PE Annexin V Apoptosis Detection Kit I (BD Biosciences). Flow cytometry was conducted on FACS-Canto or FACS-Symphony flow cytometers using BD FACS-Diva Software (BD Biosciences) for sample acquiring and FlowJo v.9.5.2 (Tree Star) for data analysis.

Bone marrow chimera experiments

Recipient mice were irradiated with a single dose of 11 Gy. Reciprocal chimeras were intravenously injected with 5 × 10^6 of donor cells. Competitive bone marrow chimeras were intravenously injected with 1:1 mixture of 5 × 10^6 of each donor cells. After 8 wk, the efficiency of hematopoietic reconstitution was assessed by quantifying the proportion of donor cells in the spleen.

Depletion of microbiota by VNAM treatment

For microbiota depletion, mice were provided with a mixture of broad-spectrum antibiotics, VNAM: 0.5 mg/ml vancomycin, 1 mg/ml neomycin, 1 mg/ml amoxicillin, and 1 mg/ml metronidazole (all Sigma-Aldrich) in drinking water ad libitum for indicated period. VNAM containing water was replaced weekly for the treatments longer than 1 wk.

FMT

The FMT solution was prepared by resuspending two fecal pellets in cold PBS in 1-ml tubes, followed by vigorous vortexing. The resulting slurry was then filtered through a 100 µm-pore

diameter nylon cell strainer (BD Falcon). Mice were given the VNAM antibiotic cocktail ad libitum in their drinking water for 4 wk. Starting 1 day after the end of VNAM treatment, mice were administered 200 µl of the FMT suspension by oral gavage for two consecutive days.

High-fat and fiber diet regimens

Mice were fed either a SD (Purina PicoLab Rodent Diet 20), a high-fat diet (D12079B; RD Western Diet), low fiber diet containing 5% cellulose (D10012M), or a high fiber diet containing 5% cellulose plus 10% soluble inulin (D19071901) for 14 days prior to ILC3 analysis. All diets were purchased from Research Diets, Inc.

C. rodentium infection

Kanamycin-resistant *C. rodentium* strain DBS120 was grown overnight at 37°C in Luria-Bertani (LB) broth supplemented with kanamycin (50 µg/ml) with vigorous shaking. The next day, 200 µl of the overnight culture was inoculated into 100 ml of fresh sterile LB broth containing Kan and incubated for 3–4 h at 37°C with vigorous shaking until reaching mid-log phase. The culture was adjusted to 1×10^{10} CFUs per mL. Mice were orally gavaged with 200 µl containing 2×10^9 CFU. Body weight was monitored every 2 days. Fecal samples were collected at defined time points after infection, weighed, and resuspended in 1 ml of sterile PBS. The samples were vortexed vigorously and allowed to settle for 10 min. Supernatants were serially diluted up to 10^{-6} and plated on LB agar plates containing Kan, followed by overnight incubation at 37°C.

C. difficile infection

The *C. difficile* VPI 10463 strain was cultured on BHI blood agar at 37°C under anaerobic conditions using BD GasPak EZ Anaerobe Container System Sachets with Indicator. Mice were pretreated with an antibiotic cocktail (0.4 mg/ml kanamycin, 0.035 mg/ml gentamicin, 0.035 mg/ml colistin, 0.215 mg/ml metronidazole, and 0.045 mg/ml vancomycin; all from Sigma-Aldrich) provided ad libitum in drinking water for 4 days. One day after completing antibiotic treatment, mice received an i.p. injection of clindamycin (10 mg/kg; Sigma-Aldrich), and the following day were infected via oral gavage with 10^8 CFU of *C. difficile* spores. Mice were weighed daily and monitored for disease severity by a blinded evaluator using a scoring system ranging from 0 (normal) to 15 (dead), based on activity, posture, coat condition, diarrhea, and ocular/nasal discharge, with each category scored from 0 to 3.

S. enterica serovar Typhimurium infection

S. typhimurium strain SL1344 engineered to express kanamycin resistance was grown overnight at 37°C in LB broth supplemented with kanamycin (50 µg/ml) with vigorous shaking. The following day, 200 µl of the overnight culture was transferred into 100 ml of fresh sterile LB with Kan and grown for additional 3–4 h at 37°C with vigorous shaking until the culture reached mid-log phase. Mice were then orally administered with 100 µl of bacterial suspension containing 1×10^7 CFU. 24 hours prior to infection, mice were pretreated with 20 mg of streptomycin sulfate solution in sterile water by oral gavage. Water and food were withdrawn 4 h before gavages; water was resumed immediately, and food was provided 2 h after infection. Body weight was assessed daily throughout the experiment. To determine fecal *S. typhimurium* burden, stool pellets were homogenized by vortexing in 1 ml of sterile PBS, allowed to settle for 10 min at RT, and the resulting supernatants were serially diluted up to 10^{-6}. The dilutions were plated on LB-Kan$^+$ agar plates and incubated at 37°C overnight. To quantify fecal *S. typhimurium* burden by qPCR, the *STM4497* gene was measured and normalized to total Eubacteria, using *E. coli* DNA to generate the standard curve. Primer sequences used are following: *STM* forward: 5′-AACAACGGCTCCGGTAATGAGATTG-3′; *STM* reverse 5′-ATGACAAACTCTTGATTCTGAAGATCG-3′; Eubacteria forward: 5′-CGGCAACGACGCCAACCC-3′; Eubacteria reverse: 5′-CCATTGTAGCACGTGTGTAGCC-3′.

RT-qPCR analysis

IEL and LP lymphocytes were isolated as described above and sorted on a BD FACS Aria II instrument. Total RNA was extracted from cells using the RNeasy Mini Kit (Qiagen, Inc.) according to the manufacturer's protocol. cDNA was synthesized from 1 µg of RNA with iScript cDNA Synthesis Kit (Bio-Rad). qPCR was performed with iTaq Universal SYBR Green Supermix (Bio-Rad) on the CFX Connect Real-Time System (BioRad). The expression of target genes was normalized to the expression of the housekeeping gene *GAPDH* and quantified using the $2^{\Delta\Delta}$Ct method. The following primers were used: *Lingo4* forward: 5′-ACTCAG ACACACGGGGAAGGTG-3′; *Lingo4* reverse: 5′-GGGTCTGGGAGG TGCAGTCAC-3′; *GAPDH* forward: 5′-CATCACTGCCACCCAGAA GACTG-3′; *GAPDH* reverse: 5′-ATGCCAGTGAGCTTCCCGTTC AG-3′.

Histological analysis of the intestinal tissue

Intestinal tissues were harvested, washed with cold PBS, opened longitudinally, and pinned out. The tissues were fixed in 10% neutral buffered formalin solution (MilliporeSigma) overnight, followed by washing in 70% ethanol and embedding in 2% agar (MilliporeSigma). Tissues were paraffin-embedded, sectioned, and stained with H&E or Alcian Blue/PAS. Stained tissue slides were scanned using the NanoZoomer-SQ Digital Slide Scanner (C13140-01; Hamamatsu Photonics K.K.). Histopathological evaluation of H&E-stained sections was performed using a 0–30 scoring system, based on the sum of 10 parameters rated from 0 (normal) to 3 (severe). The frequency of goblet cells in Alcian Blue/PAS-stained sections was assessed using a scale from 0 (absence) to 3 (enrichment). All scoring was performed by an investigator blinded to the experimental groups.

Fecal lipocalin-2 quantification

Fecal samples were reconstituted in sterile PBS with 0.1% Tween 20 at concentration of 50 mg/ml, vigorously vortexed for 20 s, followed by centrifugation at 8,000 ×*g* for 10 min. Lipocalin-2 levels were quantified using a Mouse Lipocalin-2/NGAL DuoSet ELISA kit (R&D Systems). Supernatants were diluted 4-fold to 100-fold, and absorbance was measured at 450 nm using BioTek Synergy H1 Plate Reader (Vermont, USA).

Analysis of FITC-dextran in the serum

Mice were given 0.25 mg/g of FITC-dextran (4 kDa; Sigma-Aldrich) solution in 200 µl PBS by oral gavage. After 4 h, during which mice were deprived of food and water, mice were anesthetized, and blood was collected by cardiac puncture. Presence of FITC-dextran in the serum was analyzed by spectrophotometric measurement on BioTek Synergy H1 Plate Reader (VT, USA) at 485/528 nm (excitation/emission). A standard curve was generated with serial dilutions of 100 µg/ml FITC-dextran in PBS.

In vivo antibody treatment

Uninfected, *S. typhimurium* or *C. rodentium* infected mice were i.p. injected with 150 µg anti-mouse IL-22–neutralizing antibody (clone 8E11; Genentech), 150 µg isotype control IgG2a (BioXcell), or 1 µg recombinant mouse IL-22 protein (Proteintech) in 100 µl sterile PBS at indicated time points.

Bacterial 16S rRNA quantification

Total DNA was extracted from the liver, mesenteric LNs, or fecal pellets of infected mice using the DNeasy Blood & Tissue Kit (Qiagen) as per the manufacturer's instructions. Bacterial DNA levels were quantified by qPCR with iTaq Universal SYBR Green Supermix (Bio-Rad) using primers targeting the 16S rRNA gene V4 region (forward: 5′-CGGCAACGACGCCAACCC-3′; reverse: 5′-CCATTGTAGCACGTGTGTAGCC-3′). Bacterial load was calculated using a standard curve based on serial dilutions of *E. coli* genomic DNA and expressed as 16S rRNA gene copies per gram.

Immunofluorescence

293T or 293T-Lingo4 cells were grown on coverslips overnight, washed in PBS, and fixed in 4% paraformaldehyde for 20 min at RT. Blocking and permeabilization step was conducted in PBS containing 2% BSA and 0.1% Triton X-100 for 1 h at RT. Cell were incubated with anti-FLAG antibody (#200-310-B13; Rockland) for 2 h at RT, followed by 1 h incubation with Alexa-Fluor-647 goat anti-mouse IgG (H+L) (A-21236; Invitrogen). Nuclear staining was conducted using DAPI solution (NBP2-31156; Novus Bio) for 10 min at RT. Coverslips were mounted with ProLong Glass Antifade Mountant (Invitrogen). Fluorescence images were acquired using Zeiss LSM880 Confocal Laser Scanning Microscope with Airyscan. Image analysis was performed in Fiji.

Transmission electron microscopy

ILC3s were isolated from LP as described above and sort purified on a BD FACS Aria II instrument. The cell pellet was fixed in freshly prepared 2% PFA/2.5% glutaraldehyde (Ted Pella, Inc.) in 100 mM sodium cacodylate buffer (pH 7.2) for 2 h at RT. Samples were washed in sodium cacodylate buffer, post-fixed in 1% osmium tetroxide (Ted Pella, Inc.) for 1 h, and thoroughly rinsed in dH20 before *en bloc* staining with 1% aqueous uranyl acetate (Ted Pella Inc.) for 1 h. Following additional dH2O rinses, samples were dehydrated through a graded ethanol series and embedded in Eponate 12 resin (Ted Pella Inc.). Ultrathin sections (95 nm) were cut using a Leica Ultracut UCT Ultramicrotome (Leica Microsystems Inc.) and collected on Cu grids and stained with uranyl acetate and lead citrate. Imaging was performed on a JEOL 1200 EX transmission electron microscope (JEOL USA Inc.) equipped with an AMT 8-megapixel digital camera and AMT Image Capture Engine V602 software (Advanced Microscopy Techniques). Transmission electron microscopy (TEM) analysis included at least 20 cells per sample.

Bulk RNA sequencing of ILC3s

ILC3s were isolated from LP of WT and *Lingo4*$^{-/-}$ mice as described above and sort purified on BD FACS Aria II cell sorter. Total RNA was extracted using RNeasy Mini Kits (Qiagen) as per the manufacturer's instructions. Total RNA integrity was determined using Agilent Bioanalyzer or 4200 TapeStation. Library preparation was performed using SMARTer Ultra Low RNA kit for Illumina Sequencing (Takara-Clontech) as per the manufacturer's protocol. Samples were indexed, pooled, and sequenced on an Illumina NovaSeq 6000. Base calls and demultiplexing were performed with Illumina's bcl2fastq software and a custom python demultiplexing program with a maximum of one mismatch in the indexing read. RNA-seq reads were then aligned to the Ensembl release 76 primary assembly with STAR version 2.5.1a. Gene counts were derived from the number of uniquely aligned unambiguous reads by Subread:featureCount version 1.4.6-p5. Gene count tables were processed and analyzed in R using the DESeq2 package. Before performing differential expression analysis, genes with fewer than 10 total counts across all samples were removed. Gene ontology enrichment analysis of differentially expressed genes (padj < 0.01) was carried out using Metascape (Zhou et al., 2019).

Microbiota metataxonomic analysis

Fecal samples were collected into sterile, DNA-free tubes, immediately frozen, and stored at −80°C. Microbial DNA was extracted using the PureLink Microbiome DNA Purification Kit (Thermo Fisher Scientific). Library preparation and paired-end 250 bp sequencing were performed at the Genome Access Technology Center at the McDonnell Genome Institute, Washington University in St. Louis, MO, USA, on an Illumina NovaSeq 6000 platform. Raw FASTQ files from both experiments were processed with nf-core/ampliseq v2.12.0, part of the nf-core workflow collection, using reproducible environments provided by BioConda and BioContainers. Read quality was assessed with FastQC and summarized using MultiQC. Amplicon sequence variants (ASVs) were inferred sample-wise using DADA2 (Callahan et al., 2016). Processing included removal of PhiX reads, trimming based on quality (forward and reverse reads truncated at 151 bp; reads shorter than this discarded), filtering reads with >2 expected errors, error correction, merging of paired-end reads, and chimera removal. For experiment 1 (WT vs. *Lingo4*$^{-/-}$ ± cohousing), DADA2 identified 6,610 ASVs, retaining 30.28–38.55% of reads per sample (mean 35%), corresponding to 2,450,356 total reads (130,844–167,614 per sample; mean 153,147). For experiment 2 (WT vs. *Lingo4*$^{-/-}$ at days −27, 0, 7, and 21), DADA2 identified 7,285 ASVs, retaining 27.8–60.48% of reads per sample (mean 42.7%), corresponding to 2,876,130 total reads (130–199,286 per sample; mean 119,839). Taxonomic assignment for both datasets was performed using the SILVA v138 reference database. Representative sequences, ASV

abundance tables, and taxonomy files were imported into QIIME2 (Bolyen et al., 2019). ASVs annotated as mitochondria, chloroplasts, or archaea were removed (41 removed in experiment 1; 37 removed in experiment 2), resulting in 6,569 and 7,248 ASVs, respectively, used for downstream analyses. Phylogenetic placement was performed using the SEPP fragment-insertion method with the SILVA 128 backbone, and taxonomic composition was refined using the q2-feature-classifier pretrained on SILVA 138 (99% OTUs, full-length sequences). All downstream analyses were performed in R using phyloseq, microViz, and MicrobiotaProcess. α diversity was calculated using the Shannon index, and β diversity was assessed using Bray–Curtis and unweighted UniFrac distances. Community composition, ordination plots, and taxa-level visualizations were generated with these packages. Microbiome analyses and visualization were performed in R using phyloseq (McMurdie and Holmes, 2013), microViz, and MicrobiotaProcess (Xu et al., 2023). Differential abundance testing was conducted using MaAsLin2 and LEfSe. Functional potential was inferred using PICRUSt2, producing predicted MetaCyc pathways and KEGG orthologs for downstream interpretation.

Immunoprecipitation and mass spectrometry

293T cells expressing Lingo4 with N-terminal FLAG and C-terminal 6xHis tag were lysed in cell lysis buffer (#9803; Cell Signaling) with added PMSF (#8553; Cell Signaling) for 30 min on ice, followed by centrifugation at 14,000 rpm for 10 min to collect soluble fraction. G-protein agarose beads (Sigma-Aldrich) were incubated with anti-FLAG antibody (Rockland) at concentration of 10 µg/ml in PBS for 4 h at 4°C with rotation. Preclearing of cell lysates was performed by incubation of lysates with non-coated G-protein agarose beads for 3 h with rotation at 4°C. Immunoprecipitation was conducted with anti-FLAG antibody-coated G-protein agarose beads at 4°C with rotation overnight, followed by centrifugation and washing of beads in PBS. Samples were processed using EasyPep Mini MS Sample Prep Kit (Thermo Fisher Scientific) with the following modifications: beads were washed with 100 µl 20 mM ammonium bicarbonate three times before proceeding with EasyPep Mini MS Sample Prep Kit; samples were reduced and alkylated for 30 min at 40°C, followed by 10 min at 95°C; and samples were digested overnight at 37°C with shaking (900 rpm). The extracted peptides were dried down and resuspended in water with 0.1% formic acid for LC-MS analysis. LC-MS was performed with a Dionex RSLCnano HPLC coupled to an OrbiTrap Fusion Lumos (Thermo Fisher Scientific) mass spectrometer using a 115 min gradient (1–90% acetonitrile) and 25 min re-equilibration. Sample was resolved using a 75 µm × 15 cm PepMap C18 column (Thermo Fisher Scientific) and a 75 µm × 2 cm trap column with matching stationary phase used in flow-through configuration. Sample data were analyzed using Proteome Discoverer 2.4 (Thermo Fisher Scientific). Thermo .raw files were processed using the "Spectrum Files RC" and "Spectrum Selector" nodes. Protein identifications were accepted if they could be established at >99.0% probability. Gene ontology analysis was conducted on proteins present in 239T-Lingo4 cells but not control cells and with ≥10% of coverage using Metascape (Zhou et al., 2019).

Statistical analysis

Statistical analyses were conducted using GraphPad Prism version 10.0. Survival data were analyzed using Kaplan–Meier curves and compared using the log-rank test. Normality of data distribution was assessed using the Shapiro–Wilk test, and variance homogeneity was evaluated using appropriate tests. For normally distributed datasets, two-group comparisons were performed using two-tailed unpaired Student's *t* tests, and comparisons across multiple groups were assessed using one-way ANOVA followed by Tukey's post hoc test. For non-normally distributed data, Mann–Whitney U tests were used for two-group comparisons, and the Kruskal–Wallis test with Dunn's post hoc test was applied for comparisons involving ≥ two groups. Data are presented as mean ± SEM. Statistical significance thresholds were defined as *P <0.05; **P <0.01; ***P <0.001; ****P <0.0001; ns = not significant.

Online supplemental material

Fig. S1 shows ATAC-seq data analysis of *Rorc* and *Lingo4* loci, characterizes *Lingo4* expression across lymphocyte populations and tissues, and examines the impact of *Lingo4* deficiency on intestinal lymphocyte composition. This includes *Lingo4* expression across immune compartments, analysis of RORγt$^+$ and RORγt$^-$ cells, quantification of T cell and ILC3 subsets across genetic backgrounds, cytokine production by ILC3s, and competitive bone marrow chimera experiments. Fig. S2 examines cell-intrinsic versus extrinsic effects of LINGO4 on ILC3s and evaluates microbiota composition, including reciprocal bone marrow chimeras; IL-23–induced ILC3 responses; age-dependent IL-17 production; and microbiota diversity, structure, and differentially enriched taxa under cohoused and non-cohoused conditions. Fig. S3 investigates microbiota-dependent regulation of ILC3s in *Lingo4*-deficient mice, including functional pathway predictions, dietary modulation of ILC3 frequencies, FMT outcomes, and differential microbial associations identified by multivariate analyses. Fig. S4 assesses susceptibility of *Lingo4*-deficient mice to *C. difficile* and *C. rodentium* infections across multiple genetic backgrounds, reporting disease severity, survival, bacterial burden, and weight loss under different infection paradigms. Fig. S5 evaluates host responses to *S. typhimurium* infection, including bacterial dissemination, intestinal pathology, immune cell composition, and survival outcomes in immunocompetent and lymphocyte-deficient settings. Table S1 lists proteins identified by mass spectrometry following anti-FLAG immunoprecipitation of LINGO4, highlighting interactors enriched in LINGO4-expressing cells compared with control 293T cells.

Data availability

Bulk RNA and 16S rRNA gene sequencing data generated in this study have been deposited in the Gene Expression Omnibus and are publicly available (GSE325926 and PRJNA1442760, respectively). Additional data and materials supporting the findings are available from the corresponding author upon reasonable request.

Acknowledgments

We would like to thank the Flow Cytometry and Fluorescence Activated Cell Sorting Core, the Digestive Diseases Research Core Center, the Alafi Neuroimaging Laboratory (supported by an National Institutes of Health [NIH] Shared Instrumentation grant S10 OD032131), the Molecular Microbiology Imaging Facility, and the Immunomonitoring Laboratory at the Bursky Center for Human Immunology and Immunotherapy Programs (supported by the Rheumatic Diseases Core Center, NIH WLC6313040077) at Washington University School of Medicine. We thank the Genome Technology Access Center in the Department of Genetics at Washington University School of Medicine for help with genomic analysis. The Center is partially supported by NCI Cancer Center Support Grant #P30 CA91842 to the Siteman Cancer Center and by ICTS/CTSA Grant# UL1TR000448 from the National Center for Research Resources, a component of the NIH, and NIH Roadmap for Medical Research. We thank the Bioanalytical Chemistry Facility at the Danforth Plant Science Center supported by the National Science Foundation under Grant No. DBI-1827534 for acquisition of the Orbitrap Fusion Lumos LC-MS/MS.

This study was supported by the NIH, USA (R01DK126969; R01DK132327), the Pew Charitable Trusts, USA (00035299), and the São Paulo Research Foundation, Brazil (FAPESP 2017/06577-9; 2023/00393-4).

Author contributions: José L. Fachi: conceptualization, data curation, formal analysis, funding acquisition, investigation, methodology, project administration, resources, validation, visualization, and writing—original draft, review, and editing. Tihana Trsan: formal analysis, investigation, methodology, visualization, and writing—original draft, review, and editing. Cristiane Sécca: investigation. Sarah de Oliveira: investigation. Vinícius R. Rodovalho: data curation, formal analysis, software, visualization, and writing—review and editing. Patrick Fernandes Rodrigues: investigation and methodology. Wandy L. Beatty: formal analysis, investigation, and visualization. Raki Sudan: investigation. Shitong Wu: formal analysis. Bishan Bhattarai: investigation. Santosh K. Panda: data curation, investigation, methodology, and resources. Marina Cella: conceptualization, supervision, and writing—review and editing. Susan Gilfillan: methodology and resources. Marco Colonna: conceptualization, funding acquisition, project administration, and writing—review and editing.

Disclosures: The authors declare no competing interests exist.

Submitted: 18 December 2025
Revised: 27 February 2026
Accepted: 1 April 2026

References

Abt, M.C., B.B. Lewis, S. Caballero, H. Xiong, R.A. Carter, B. Sušac, L. Ling, I. Leiner, and E.G. Pamer. 2015. Innate immune defenses mediated by two ILC subsets are critical for protection against acute clostridium difficile infection. *Cell Host Microbe*. 18:27–37. https://doi.org/10.1016/j.chom.2015.06.011

Abt, M.C., P.T. McKenney, and E.G. Pamer. 2016. Clostridium difficile colitis: Pathogenesis and host defence. *Nat. Rev. Microbiol.* 14:609–620. https://doi.org/10.1038/nrmicro.2016.108

Behnsen, J., S. Jellbauer, C.P. Wong, R.A. Edwards, M.D. George, W. Ouyang, and M. Raffatellu. 2014. The cytokine IL-22 promotes pathogen colonization by suppressing related commensal bacteria. *Immunity*. 40:262–273. https://doi.org/10.1016/j.immuni.2014.01.003

Belle, N.M., Y. Ji, K. Herbine, Y. Wei, J. Park, K. Zullo, L.-Y. Hung, S. Srivatsa, T. Young, T. Oniskey, et al. 2019. TFF3 interacts with LINGO2 to regulate EGFR activation for protection against colitis and gastrointestinal helminths. *Nat. Commun.* 10:4408. https://doi.org/10.1038/s41467-019-12315-1

Bolyen, E., J.R. Rideout, M.R. Dillon, N.A. Bokulich, C.C. Abnet, G.A. Al-Ghalith, H. Alexander, E.J. Alm, M. Arumugam, F. Asnicar, et al. 2019. Reproducible, interactive, scalable and extensible microbiome data science using QIIME 2. *Nat. Biotechnol.* 37:852–857. https://doi.org/10.1038/s41587-019-0209-9

Buonocore, S., P.P. Ahern, H.H. Uhlig, I.I. Ivanov, D.R. Littman, K.J. Maloy, and F. Powrie. 2010. Innate lymphoid cells drive interleukin-23-dependent innate intestinal pathology. *Nature*. 464:1371–1375. https://doi.org/10.1038/nature08949

Callahan, B.J., P.J. McMurdie, M.J. Rosen, A.W. Han, A.J.A. Johnson, and S.P. Holmes. 2016. DADA2: High-resolution sample inference from Illumina amplicon data. *Nat. Methods*. 13:581–583. https://doi.org/10.1038/nmeth.3869

Cella, M., A. Fuchs, W. Vermi, F. Facchetti, K. Otero, J.K.M. Lennerz, J.M. Doherty, J.C. Mills, and M. Colonna. 2009. A human natural killer cell subset provides an innate source of IL-22 for mucosal immunity. *Nature*. 457:722–725. https://doi.org/10.1038/nature07537

Chen, X., K. Katchar, J.D. Goldsmith, N. Nanthakumar, A. Cheknis, D.N. Gerding, and C.P. Kelly. 2008. A mouse model of clostridium difficile-associated disease. *Gastroenterology*. 135:1984–1992. https://doi.org/10.1053/j.gastro.2008.09.002

Chun, E., S. Lavoie, D. Fonseca-Pereira, S. Bae, M. Michaud, H.R. Hoveyda, G.L. Fraser, C.A. Gallini Comeau, J.N. Glickman, M.H. Fuller, et al. 2019. Metabolite-sensing receptor Ffar2 regulates colonic group 3 innate lymphoid cells and gut immunity. *Immunity*. 51:871–884.e6. https://doi.org/10.1016/j.immuni.2019.09.014

Clay, S.L., A. Bravo-Blas, D.M. Wall, M.K.L. MacLeod, and S.W.F. Milling. 2020. Regulatory T cells control the dynamic and site-specific polarization of total CD4 T cells following Salmonella infection. *Mucosal Immunol.* 13:946–957. https://doi.org/10.1038/s41385-020-0299-1

Collins, J.W., K.M. Keeney, V.F. Crepin, V.A.K. Rathinam, K.A. Fitzgerald, B.B. Finlay, and G. Frankel. 2014. Citrobacter rodentium: Infection, inflammation and the microbiota. *Nat. Rev. Microbiol.* 12:612–623. https://doi.org/10.1038/nrmicro3315

Cupedo, T., N.K. Crellin, N. Papazian, E.J. Rombouts, K. Weijer, J.L. Grogan, W.E. Fibbe, J.J. Cornelissen, and H. Spits. 2009. Human fetal lymphoid tissue-inducer cells are interleukin 17-producing precursors to RORC+ CD127+ natural killer-like cells. *Nat. Immunol.* 10:66–74. https://doi.org/10.1038/ni.1668

Di Luccia, B., S. Gilfillan, M. Cella, M. Colonna, and S.C.-C. Huang. 2019. ILC3s integrate glycolysis and mitochondrial production of reactive oxygen species to fulfill activation demands. *J. Exp. Med.* 216:2231–2241. https://doi.org/10.1084/jem.20180549

Dudem, S., R.J. Large, S. Kulkarni, H. McClafferty, I.G. Tikhonova, G.P. Sergeant, K.D. Thornbury, M.J. Shipston, B.A. Perrino, and M.A. Hollywood. 2020. LINGO1 is a regulatory subunit of large conductance, Ca^{2+}-activated potassium channels. *Proc. Natl. Acad. Sci. USA*. 117:2194–2200. https://doi.org/10.1073/pnas.1916715117

Eberl, G., M. Colonna, J.P. Di Santo, and A.N.J. McKenzie. 2015. Innate lymphoid cells. Innate lymphoid cells: A new paradigm in immunology. *Science*. 348:aaa6566. https://doi.org/10.1126/science.aaa6566

Eberl, G., S. Marmon, M.-J. Sunshine, P.D. Rennert, Y. Choi, and D.R. Littman. 2004. An essential function for the nuclear receptor RORgamma(t) in the generation of fetal lymphoid tissue inducer cells. *Nat. Immunol.* 5:64–73. https://doi.org/10.1038/ni1022

Fachi, J.L., B. Di Luccia, S. Gilfillan, H.-W. Chang, C. Song, J. Cheng, M. Cella, M.A. Vinolo, J.I. Gordon, and M. Colonna. 2024. Deficiency of IL-22-binding protein enhances the ability of the gut microbiota to protect against enteric pathogens. *Proc. Natl. Acad. Sci. USA*. 121:e2321836121. https://doi.org/10.1073/pnas.2321836121

Fachi, J.L., S. de Oliveira, T. Trsan, S. Penati, S. Gilfillan, S. Cao, P. Ribeiro Castro, M.F. Fernandes, K.L. Hyrc, X. Liu, et al. 2025. Fiber- and acetate-mediated modulation of MHC-II expression on intestinal epithelium protects from Clostridioides difficile infection. *Cell Host Microbe*. 33:235–251.e7. https://doi.org/10.1016/j.chom.2024.12.017

Fachi, J.L., C. Sécca, P.B. Rodrigues, F.C.P. de Mato, B. Di Luccia, J.S. Felipe, L.P. Pral, M. Rungue, V.M. Rocha, F.T. Sato, et al. 2020. Acetate coordinates neutrophil and ILC3 responses against C. difficile through FFAR2. *J. Exp. Med.* 217:20190489. https://doi.org/10.1084/jem.20190489

Faria, A.M.C., B.S. Reis, and D. Mucida. 2017. Tissue adaptation: Implications for gut immunity and tolerance. *J. Exp. Med.* 214:1211–1226. https://doi.org/10.1084/jem.20162014

Fonseca-Pereira, D., S. Bae, S.L. Clay, M. Michaud, M.H. MacDonald, J.N. Glickman, and W.S. Garrett. 2025. The metabolic sensor LKB1 regulates ILC3 homeostasis and mitochondrial function. *Cell Rep.* 44:115456. https://doi.org/10.1016/j.celrep.2025.115456

Grizotte-Lake, M., G. Zhong, K. Duncan, J. Kirkwood, N. Iyer, I. Smolenski, N. Isoherranen, and S. Vaishnava. 2018. Commensals suppress intestinal epithelial cell retinoic acid synthesis to regulate interleukin-22 activity and prevent microbial dysbiosis. *Immunity*. 49:1103–1115.e6. https://doi.org/10.1016/j.immuni.2018.11.018

Guillemain, A., Y. Laouarem, L. Cobret, D. Štefok, W. Chen, S. Bloch, A. Zahaf, L. Blot, F. Reverchon, T. Normand, et al. 2020. LINGO family receptors are differentially expressed in the mouse brain and form native multimeric complexes. *FASEB J.* 34:13641–13653. https://doi.org/10.1096/fj.202000826R

Guo, X., J. Qiu, T. Tu, X. Yang, L. Deng, R.A. Anders, L. Zhou, and Y.-X. Fu. 2014. Induction of innate lymphoid cell-derived interleukin-22 by the transcription factor STAT3 mediates protection against intestinal infection. *Immunity*. 40:25–39. https://doi.org/10.1016/j.immuni.2013.10.021

Gury-BenAri, M., C.A. Thaiss, N. Serafini, D.R. Winter, A. Giladi, D. Lara-Astiaso, M. Levy, T.M. Salame, A. Weiner, E. David, et al. 2016. The spectrum and regulatory landscape of intestinal innate lymphoid cells are shaped by the microbiome. *Cell*. 166:1231–1246.e13. https://doi.org/10.1016/j.cell.2016.07.043

Haines, B.P., and P.W.J. Rigby. 2008. Expression of the Lingo/LERN gene family during mouse embryogenesis. *Gene Expr. Patterns.* 8:79–86. https://doi.org/10.1016/j.modgep.2007.10.003

He, Y.W., M.L. Deftos, E.W. Ojala, and M.J. Bevan. 1998. RORgamma t, a novel isoform of an orphan receptor, negatively regulates Fas ligand expression and IL-2 production in T cells. *Immunity*. 9:797–806. https://doi.org/10.1016/s1074-7613(00)80645-7

Heng, T.S.P., M.W. Painter, and Immunological Genome Project Consortium. 2008. The immunological genome Project: Networks of gene expression in immune cells. *Nat. Immunol.* 9:1091–1094. https://doi.org/10.1038/ni1008-1091

Horn, V., and G.F. Sonnenberg. 2024. Group 3 innate lymphoid cells in intestinal health and disease. *Nat. Rev. Gastroenterol. Hepatol.* 21:428–443. https://doi.org/10.1038/s41575-024-00906-3

Hou, Q., J. Huang, X. Xiong, Y. Guo, and B. Zhang. 2022. Role of nutrient-sensing receptor GPRC6A in regulating colonic group 3 innate lymphoid cells and inflamed mucosal healing. *J. Crohns Colitis.* 16:1293–1305. https://doi.org/10.1093/ecco-jcc/jjac020

Inoue, H., L. Lin, X. Lee, Z. Shao, S. Mendes, P. Snodgrass-Belt, H. Sweigard, T. Engber, B. Pepinsky, L. Yang, et al. 2007. Inhibition of the leucine-rich repeat protein LINGO-1 enhances survival, structure, and function of dopaminergic neurons in Parkinson's disease models. *Proc. Natl. Acad. Sci. USA*. 104:14430–14435. https://doi.org/10.1073/pnas.0700901104

Jarade, A., Z. Garcia, S. Marie, A. Demera, I. Prinz, P. Bousso, J.P. Di Santo, and N. Serafini. 2022. Inflammation triggers ILC3 patrolling of the intestinal barrier. *Nat. Immunol.* 23:1317–1323. https://doi.org/10.1038/s41590-022-01284-1

Kabil, A.K., L.T. Liu, C. Xu, N. Nayyar, L. González, S. Chopra, J. Brassard, M.-J. Beaulieu, Y. Li, A. Damji, et al. 2025. Microbial dysbiosis sculpts a systemic ILC3/IL-17 axis governing lung inflammatory responses and central hematopoiesis. *Mucosal Immunol.* 18:1139–1158. https://doi.org/10.1016/j.mucimm.2025.07.002

Kiss, E.A., C. Vonarbourg, S. Kopfmann, E. Hobeika, D. Finke, C. Esser, and A. Diefenbach. 2011. Natural aryl hydrocarbon receptor ligands control organogenesis of intestinal lymphoid follicles. *Science* 334:1561–1565. https://doi.org/10.1126/science.1214914

Klose, C.S.N., and D. Artis. 2016. Innate lymphoid cells as regulators of immunity, inflammation and tissue homeostasis. *Nat. Immunol.* 17:765–774. https://doi.org/10.1038/ni.3489

Lee, J.S., M. Cella, K.G. McDonald, C. Garlanda, G.D. Kennedy, M. Nukaya, A. Mantovani, R. Kopan, C.A. Bradfield, R.D. Newberry, and M. Colonna. 2011. AHR drives the development of gut ILC22 cells and postnatal lymphoid tissues via pathways dependent on and independent of Notch. *Nat. Immunol.* 13:144–151. https://doi.org/10.1038/ni.2187

Lehmann, F.M., N. von Burg, R. Ivanek, C. Teufel, E. Horvath, A. Peter, G. Turchinovich, D. Staehli, T. Eichlisberger, M. Gomez de Agüero, et al. 2020. Microbiota-induced tissue signals regulate ILC3-mediated antigen presentation. *Nat. Commun.* 11:1794. https://doi.org/10.1038/s41467-020-15612-2

Li, N., V. van Unen, T. Höllt, A. Thompson, J. van Bergen, N. Pezzotti, E. Eisemann, A. Vilanova, S.M. Chuva de Sousa Lopes, B.P.F. Lelieveldt, and F. Koning. 2018. Mass cytometry reveals innate lymphoid cell differentiation pathways in the human fetal intestine. *J. Exp. Med.* 215:1383–1396. https://doi.org/10.1084/jem.20171934

Liang, S.C., X.-Y. Tan, D.P. Luxenberg, R. Karim, K. Dunussi-Joannopoulos, M. Collins, and L.A. Fouser. 2006. Interleukin (IL)-22 and IL-17 are coexpressed by Th17 cells and cooperatively enhance expression of antimicrobial peptides. *J. Exp. Med.* 203:2271–2279. https://doi.org/10.1084/jem.20061308

Lo, B.C., D. Canals Hernaez, R.W. Scott, M.R. Hughes, S.B. Shin, T.M. Underhill, F. Takei, and K.M. McNagny. 2019. The transcription factor RORα preserves ILC3 lineage identity and function during chronic intestinal infection. *J. Immunol.* 203:3209–3215. https://doi.org/10.4049/jimmunol.1900781

McMurdie, P.J., and S. Holmes. 2013. Phyloseq: an R package for reproducible interactive analysis and graphics of microbiome census data. *PLoS One*. 8:e61217. https://doi.org/10.1371/journal.pone.0061217

Mi, S., B. Hu, K. Hahm, Y. Luo, E.S. Kam Hui, Q. Yuan, W.M. Wong, L. Wang, H. Su, T.-H. Chu, et al. 2007. LINGO-1 antagonist promotes spinal cord remyelination and axonal integrity in MOG-induced experimental autoimmune encephalomyelitis. *Nat. Med.* 13:1228–1233. https://doi.org/10.1038/nm1664

Pedicord, V.A., A.A.K. Lockhart, K.J. Rangan, J.W. Craig, J. Loschko, A. Rogoz, H.C. Hang, and D. Mucida. 2016. Exploiting a host-commensal interaction to promote intestinal barrier function and enteric pathogen tolerance. *Sci. Immunol.* 1:eaai7732. https://doi.org/10.1126/sciimmunol.aai7732

Pral, L.P., J.L. Fachi, R.O. Corrêa, M. Colonna, and M.A.R. Vinolo. 2021. Hypoxia and HIF-1 as key regulators of gut microbiota and host interactions. *Trends Immunol.* 42:604–621. https://doi.org/10.1016/j.it.2021.05.004

Reynders, A., N. Yessaad, T.-P. Vu Manh, M. Dalod, A. Fenis, C. Aubry, G. Nikitas, B. Escalière, J.C. Renauld, O. Dussurget, et al. 2011. Identity, regulation and in vivo function of gut NKp46+RORγt+ and NKp46+RORγt- lymphoid cells. *EMBO J.* 30:2934–2947. https://doi.org/10.1038/emboj.2011.201

Rodrigues, P.F., S. Wu, T. Trsan, S.K. Panda, J.L. Fachi, Y. Liu, S. Du, S. de Oliveira, A.U. Antonova, D. Khantakova, et al. 2025. Rorγt-positive dendritic cells are required for the induction of peripheral regulatory T cells in response to oral antigens. *Cell*. 188:2720–2737.e22. https://doi.org/10.1016/j.cell.2025.03.02

Sabihi, M., M. Böttcher, P. Pelczar, and S. Huber. 2020. Microbiota-dependent effects of IL-22. *Cells*. 9:2205. https://doi.org/10.3390/cells9102205

Sanos, S.L., V.L. Bui, A. Mortha, K. Oberle, C. Heners, C. Johner, and A. Diefenbach. 2009. RORgammat and commensal microflora are required for the differentiation of mucosal interleukin 22-producing NKp46+ cells. *Nat. Immunol.* 10:83–91. https://doi.org/10.1038/ni.1684

Satoh-Takayama, N., C.A.J. Vosshenrich, S. Lesjean-Pottier, S. Sawa, M. Lochner, F. Rattis, J.-J. Mention, K. Thiam, N. Cerf-Bensussan, O. Mandelboim, et al. 2008. Microbial flora drives interleukin 22 production in intestinal NKp46+ cells that provide innate mucosal immune defense. *Immunity*. 29:958–970. https://doi.org/10.1016/j.immuni.2008.11.001

Sawa, S., M. Cherrier, M. Lochner, N. Satoh-Takayama, H.J. Fehling, F. Langa, J.P. Di Santo, and G. Eberl. 2010. Lineage relationship analysis of RORgammat+ innate lymphoid cells. *Science*. 330:665–669. https://doi.org/10.1126/science.1194597

Serafini, N., C.A.J. Vosshenrich, and J.P. Di Santo. 2015. Transcriptional regulation of innate lymphoid cell fate. *Nat. Rev. Immunol.* 15:415–428. https://doi.org/10.1038/nri3855

Sonnenberg, G.F., L.A. Fouser, and D. Artis. 2011. Border patrol: Regulation of immunity, inflammation and tissue homeostasis at barrier surfaces by IL-22. *Nat. Immunol.* 12:383–390. https://doi.org/10.1038/ni.2025

Sun, Z., D. Unutmaz, Y.R. Zou, M.J. Sunshine, A. Pierani, S. Brenner-Morton, R.E. Mebius, and D.R. Littman. 2000. Requirement for RORgamma in

thymocyte survival and lymphoid organ development. *Science*. 288: 2369–2373. https://doi.org/10.1126/science.288.5475.2369

Teufel, C., E. Horvath, A. Peter, C. Ercan, S. Piscuoglio, M.N. Hall, D. Finke, and F.M. Lehmann. 2021. mTOR signaling mediates ILC3-driven immunopathology. *Mucosal Immunol.* 14:1323–1334. https://doi.org/10.1038/s41385-021-00432-4

van de Pavert, S.A., M. Ferreira, R.G. Domingues, H. Ribeiro, R. Molenaar, L. Moreira-Santos, F.F. Almeida, S. Ibiza, I. Barbosa, G. Goverse, et al. 2014. Maternal retinoids control type 3 innate lymphoid cells and set the offspring immunity. *Nature*. 508:123–127. https://doi.org/10.1038/nature13158

van der Velden, A.W.M., M.K. Copass, and M.N. Starnbach. 2005. Salmonella inhibit T cell proliferation by a direct, contact-dependent immunosuppressive effect. *Proc. Natl. Acad. Sci. USA*. 102:17769–17774. https://doi.org/10.1073/pnas.0504382102

Vivier, E., D. Artis, M. Colonna, A. Diefenbach, J.P. Di Santo, G. Eberl, S. Koyasu, R.M. Locksley, A.N.J. McKenzie, R.E. Mebius, et al. 2018. Innate lymphoid cells: 10 years on. *Cell*. 174:1054–1066. https://doi.org/10.1016/j.cell.2018.07.017

Walker, G.T., R.R. Gerner, S.-P. Nuccio, and M. Raffatellu. 2023. Murine models of Salmonella infection. *Curr. Protoc.* 3:e824. https://doi.org/10.1002/cpz1.824

Wang, R., W. Cui, and H. Yang. 2023. The interplay between innate lymphoid cells and microbiota. *mBio*. 14:e0039923. https://doi.org/10.1128/mbio.00399-23

Wang, X., M.H. Yan, H. Fujioka, J. Liu, A. Wilson-Delfosse, S.G. Chen, G. Perry, G. Casadesus, and X. Zhu. 2012. LRRK2 regulates mitochondrial dynamics and function through direct interaction with DLP1. *Hum. Mol. Genet.* 21:1931–1944. https://doi.org/10.1093/hmg/dds003

Weindel, C.G., S.L. Bell, K.J. Vail, K.O. West, K.L. Patrick, and R.O. Watson. 2020. LRRK2 maintains mitochondrial homeostasis and regulates innate immune responses to Mycobacterium tuberculosis. *Elife*. 9:e51071. https://doi.org/10.7554/eLife.51071

Wu, D., L. Hu, M. Han, Y. Deng, Y. Zhang, G. Ren, X. Zhao, Z. Li, P. Li, Y. Zhang, et al. 2022. PD-1 signaling facilitates activation of lymphoid tissue inducer cells by restraining fatty acid oxidation. *Nat. Metab.* 4: 867–882. https://doi.org/10.1038/s42255-022-00595-9

Xiong, L., S. Wang, J.W. Dean, K.N. Oliff, C. Jobin, R. Curtiss, and L. Zhou. 2022. Group 3 innate lymphoid cell pyroptosis represents a host defence mechanism against Salmonella infection. *Nat. Microbiol.* 7:1087–1099. https://doi.org/10.1038/s41564-022-01142-8

Xu, S., L. Zhan, W. Tang, Q. Wang, Z. Dai, L. Zhou, T. Feng, M. Chen, T. Wu, E. Hu, and G. Yu. 2023. MicrobiotaProcess: A comprehensive R package for deep mining microbiome. *Innovation (Camb.)*. 4:100388. https://doi.org/10.1016/j.xinn.2023.100388

Yu, H., N. Jacquelot, and G.T. Belz. 2022. Metabolic features of innate lymphoid cells. *J. Exp. Med.* 219:e20221140. https://doi.org/10.1084/jem.20221140

Zenewicz, L.A., X. Yin, G. Wang, E. Elinav, L. Hao, L. Zhao, and R.A. Flavell. 2013. IL-22 deficiency alters colonic microbiota to be transmissible and colitogenic. *J. Immunol.* 190:5306–5312. https://doi.org/10.4049/jimmunol.1300016

Zheng, Y., P.A. Valdez, D.M. Danilenko, Y. Hu, S.M. Sa, Q. Gong, A.R. Abbas, Z. Modrusan, N. Ghilardi, F.J. de Sauvage, and W. Ouyang. 2008. Interleukin-22 mediates early host defense against attaching and effacing bacterial pathogens. *Nat. Med.* 14:282–289. https://doi.org/10.1038/nm1720

Zhou, Y., B. Zhou, L. Pache, M. Chang, A.H. Khodabakhshi, O. Tanaseichuk, C. Benner, and S.K. Chanda. 2019. Metascape provides a biologist-oriented resource for the analysis of systems-level datasets. *Nat. Commun.* 10: 1523. https://doi.org/10.1038/s41467-019-09234-6

Zhu, Q., D. Korenfeld, A. Suarez-Fueyo, S. Graham, L. Jin, S. Punit, R. Duffy, M. Puri, A. Caruso, C. Hu, et al. 2022. Epithelial dysfunction is prevented by IL-22 treatment in a Citrobacter rodentium-induced colitis model that shares similarities with inflammatory bowel disease. *Mucosal Immunol.* 15:1338–1349. https://doi.org/10.1038/s41385-022-00577-w

Zindl, C.L., C.G. Wilson, A.S. Chadha, L.W. Duck, B. Cai, S.N. Harbour, Y. Nagaoka-Kamata, R.D. Hatton, M. Gao, D.A. Figge, and C.T. Weaver. 2024. Distal colonocytes targeted by C. rodentium recruit T-cell help for barrier defence. *Nature*. 629:669–678. https://doi.org/10.1038/s41586-024-07288-1

Zullo, K.M., B. Douglas, N.M. Maloney, Y. Ji, Y. Wei, K. Herbine, R. Cohen, C. Pastore, Z. Cramer, X. Wang, et al. 2021. LINGO3 regulates mucosal tissue regeneration and promotes TFF2 dependent recovery from colitis. *Scand. J. Gastroenterol.* 56:791–805. https://doi.org/10.1080/00365521.2021.1917650

JEM

Supplemental material

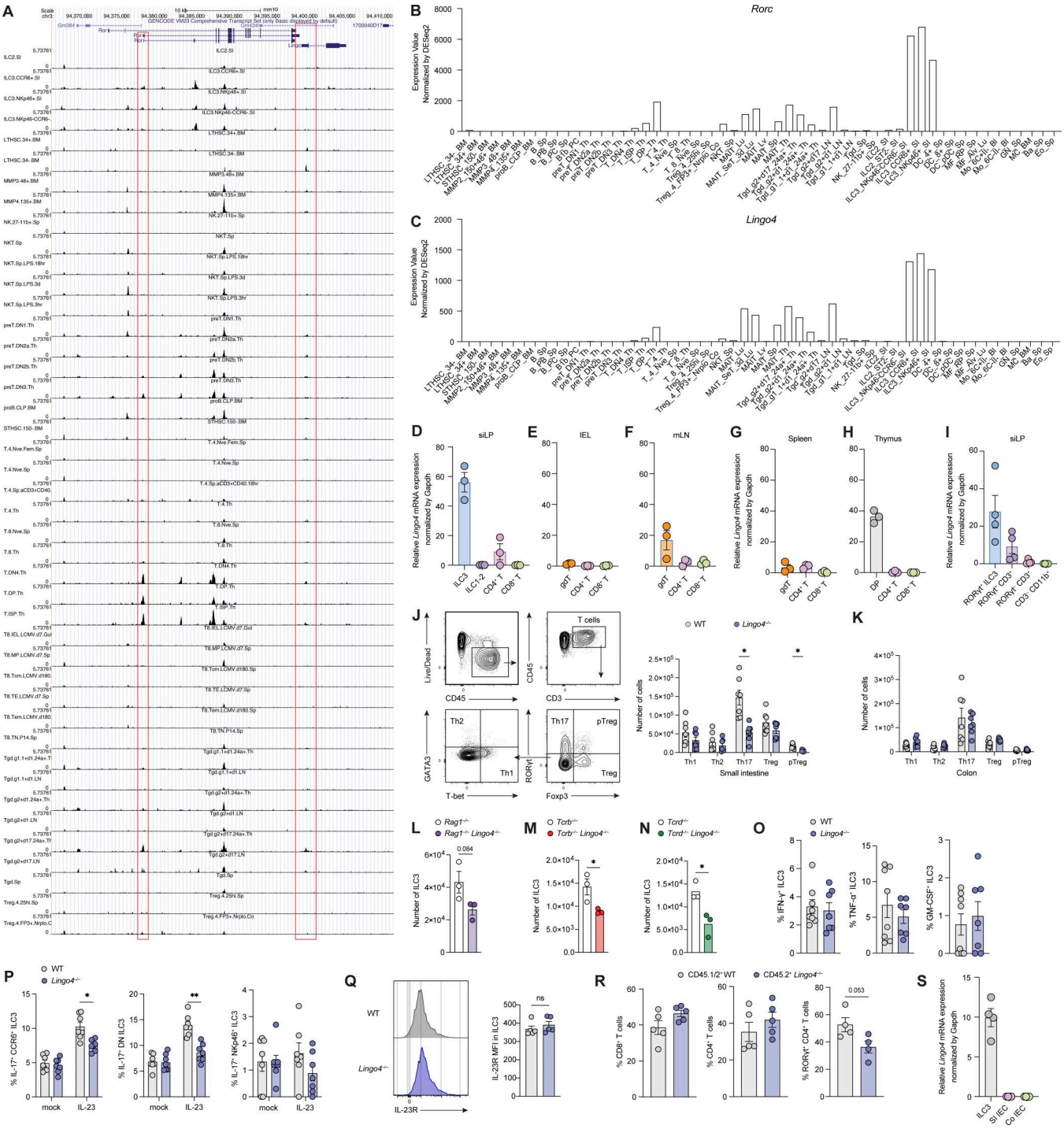

Figure S1. ***Lingo4* expression across lymphocyte populations and tissues (related to Fig. 1). (A)** Analysis of ImmGen ATAC-seq data across annotated mouse lymphocyte populations showing coordinated chromatin accessibility at the *Rorc* and *Lingo4* loci. **(B and C)** Expression of *Rorc* (B) and *Lingo4* (C) across annotated mouse lymphocyte populations based on data from ImmGen consortium. **(D–H)** Expression of *Lingo4* in lymphocytes sorted from siLP (D), IELs (E), mesenteric LNs (mLNs) (F), spleen (G), and thymus (H). Mean ± SEM, *n* = 3. **(I)** *Lingo4* expression in RORγt$^+$ and RORγt$^-$ cells sorted from siLP of *Rorc*^{GFP} mice. Mean ± SEM, *n* = 4. **(J and K)** Gating strategy and absolute numbers of T cell subsets in the siLP (J) and colon (K) of WT and *Lingo4*$^{-/-}$ mice. Th1, Tbet$^+$ T cells; Th2, GATA3$^+$ T cells; Th17, RORγt$^+$ T cells; Treg, Foxp3$^+$ T cells; and pTreg, RORγt$^+$ Foxp3$^+$ T cells. Mean ± SEM, *n* = 7–12; pooled from three independent experiments. **(L–N)** Numbers of ILC3s in siLP of WT and *Lingo4*$^{-/-}$ mice on *Rag1*$^{-/-}$ (L), *Tcrb*$^{-/-}$ (M), and *Tcrd*$^{-/-}$ (N) backgrounds. Mean ± SEM, *n* = 3. **(O)** Percentage of IFN-γ$^+$, TNF-α$^+$, and GM-CSF$^+$ ILC3s from siLP of WT and *Lingo4*$^{-/-}$ mice. Mean ± SEM, *n* = 8; two experiments combined. **(P)** IL17 production by across siLP ILC3 subsets. Mean ± SEM, *n* = 7. Two experiments combined. **(Q)** Flow cytometry analysis of IL-23R expression between WT and *Lingo4*$^{-/-}$ ILC3s. Mean ± SEM, *n* = 5. **(R)** Frequencies of WT (CD45.1/2$^+$) and *Lingo4*$^{-/-}$ (CD45.2$^+$) T cell subsets in siLP 8 wk after bone marrow reconstitution of irradiated CD45.1$^+$ mice. Mean ± SEM, *n* = 4–5; two experiments combined. **(S)** Expression of *Lingo4* in intestinal epithelial cells sorted from siLP or colon and compared with siLP ILC3s. Mean ± SEM, *n* = 5. **(D–S)** Statistical significance was assessed using unpaired two-tailed *t* tests or one-way ANOVA with Tukey's post hoc test. *P < 0.05; **P < 0.01.

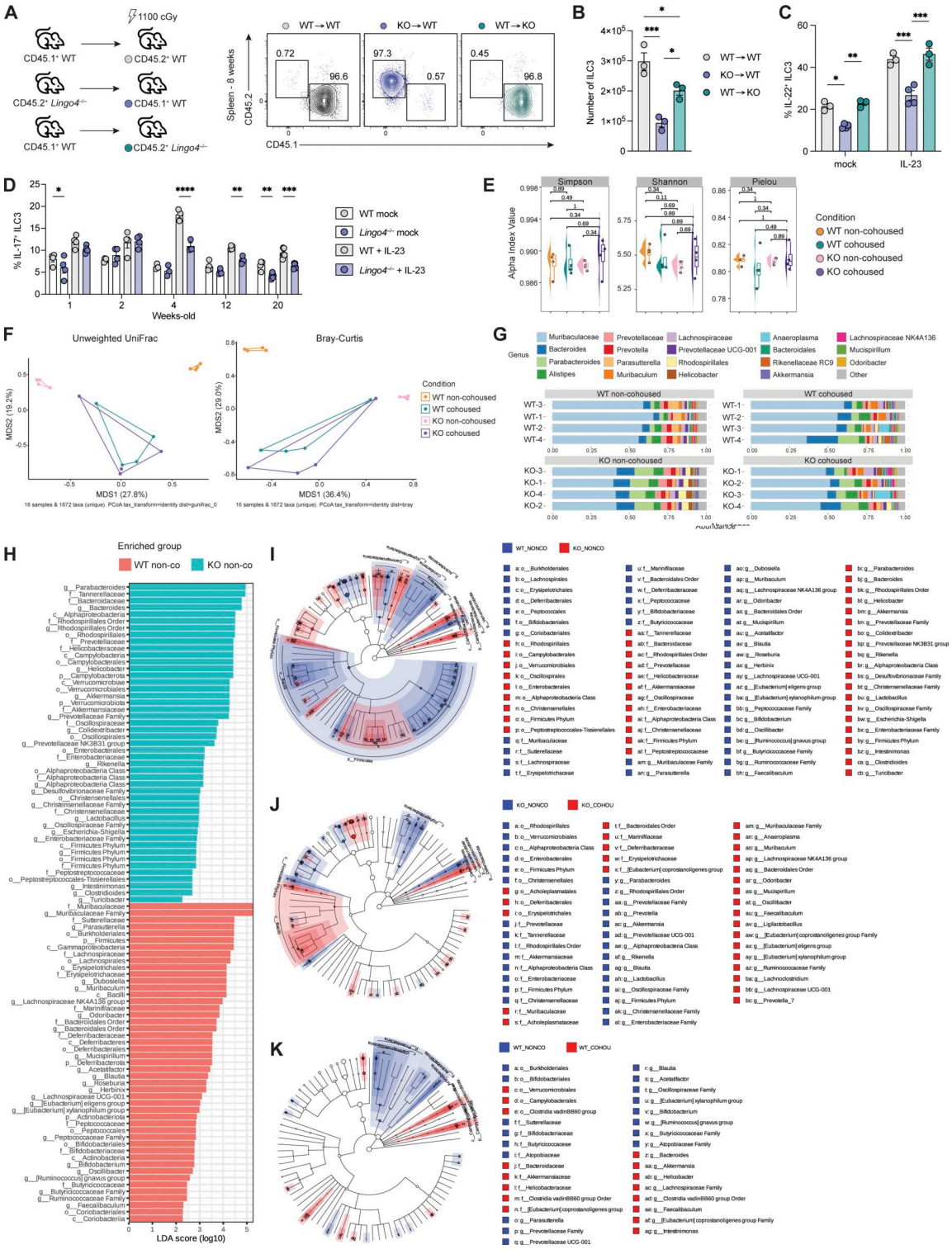

Figure S2. **Effects of *Lingo4* deficiency on intestinal lymphocytes and microbiota composition (related to Fig. 2). (A)** Reciprocal BM chimeras: irradiated WT or *Lingo4*$^{-/-}$ mice were reconstituted with WT or *Lingo4*$^{-/-}$ BM, as indicated. Representative spleen reconstitution after 8 wk. *n* = 3; representative of two experiments. **(B and C)** Frequencies of ILC3s in siLP (B) and IL-22^{+} ILC3s (C) after IL-23 stimulation in mice shown in A. Mean ± SEM, *n* = 3; representative of two experiments. **(D)** Frequencies of IL-17^{+} ILC3s following IL-23 stimulation in WT and *Lingo4*$^{-/-}$ mice across ages. Mean ± SEM, *n* = 4–5. **(E)** Microbiota α-diversity of cohoused and non-cohoused WT and *Lingo4*$^{-/-}$ mice by Shannon, Simpson, and Pielou indices. *n* = 4. **(F and G)** Multidimensional scaling (MDS) plots of cohoused vs. non-cohoused WT and *Lingo4*$^{-/-}$ mice based on Unweighted UniFrac and Bray–Curtis distances (F) and relative genus-level abundance (G). *n* = 4. **(H)** Differentially enriched taxa identified by LEfSe analysis in non-cohoused T and *Lingo4*$^{-/-}$ mice represented by LDA score. *n* = 4. **(I–K)** LEfSe-identified differentially enriched taxa for non-cohoused WT vs. *Lingo4*$^{-/-}$ mice (I), cohoused vs. non-cohoused *Lingo4*$^{-/-}$ mice (J), and cohoused vs. non-cohoused WT mice (K). *n* = 4. **(A–D)** Statistical significance was assessed using one-way ANOVA with Tukey's post hoc test. *P < 0.05; **P < 0.01; ***P < 0.001; ****P < 0.0001.

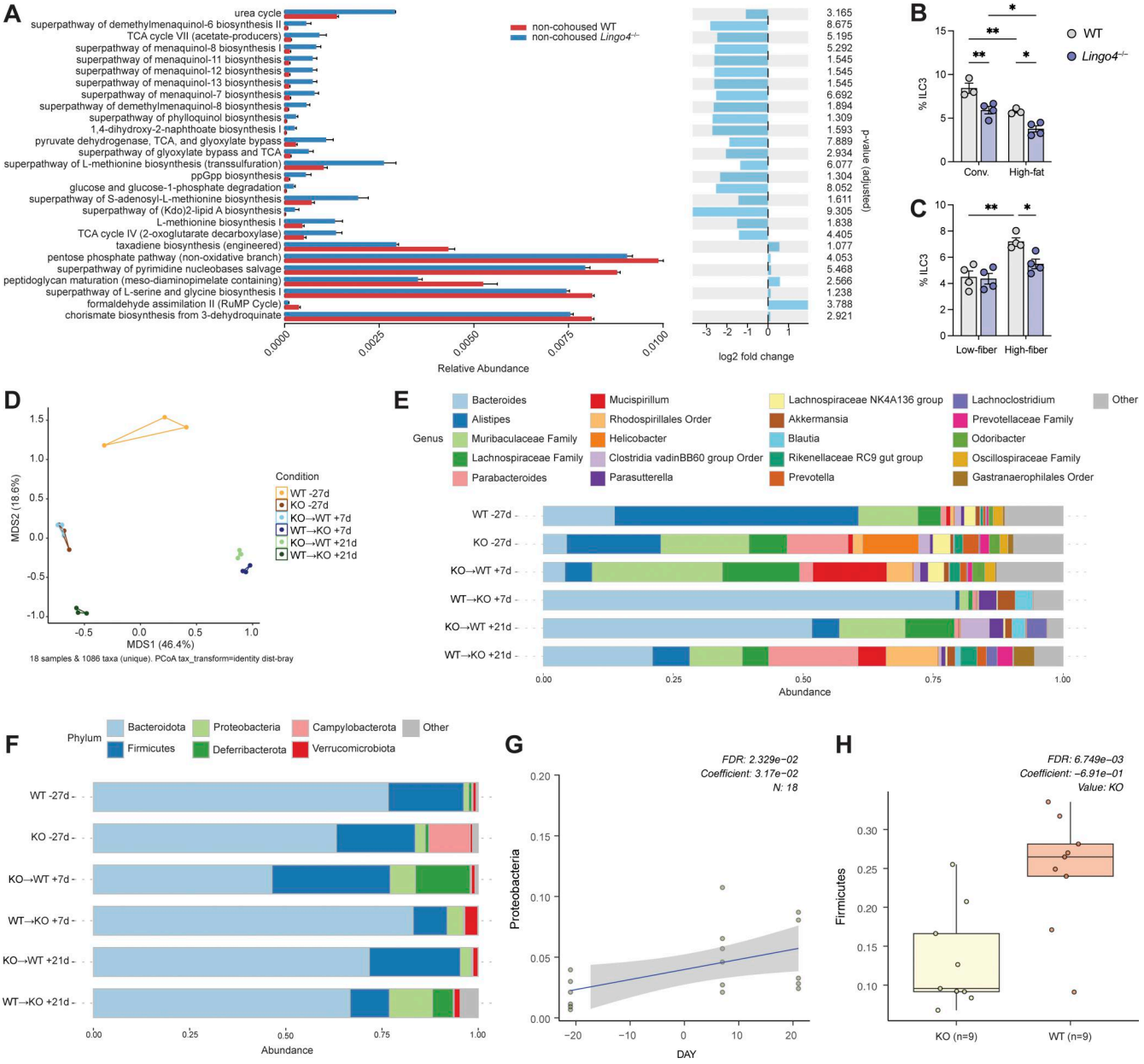

Figure S3. **Microbiota-dependent regulation of ILC3s in *Lingo4*-deficient mice (related to Fig. 3). (A)** Functional pathway predictions generated using PICRUSt2 based on 16S rRNA gene sequencing of non-cohoused WT vs. *Lingo4*$^{-/-}$ mice. *n* = 4. **(B and C)** Frequencies of ILC3s in siLP of WT and *Lingo4*$^{-/-}$ mice fed with high-fat (B) or low- or high-fiber diets (C). Mean ± SEM, *n* = 3–4; representative of two experiments. **(D)** MDS plot of WT and *Lingo4*$^{-/-}$ mice after FMT based on Bray–Curtis distances. *n* = 4. **(E and F)** Relative abundances at genus (E) and phylum (F) levels from samples shown in D. *n* = 4. **(G and H)** Differential abundance analysis by MaAsLin2 following FMT: association of Proteobacteria with time post-FMT in *Lingo4*$^{-/-}$ mice (G); association of Firmicutes with genotype (WT vs. *Lingo4*$^{-/-}$) (H). *n* = 4. **(B and C)** Statistical significance was assessed using one-way ANOVA with Tukey's post hoc test. *P < 0.05; **P < 0.01. MDS, multidimensional scaling.

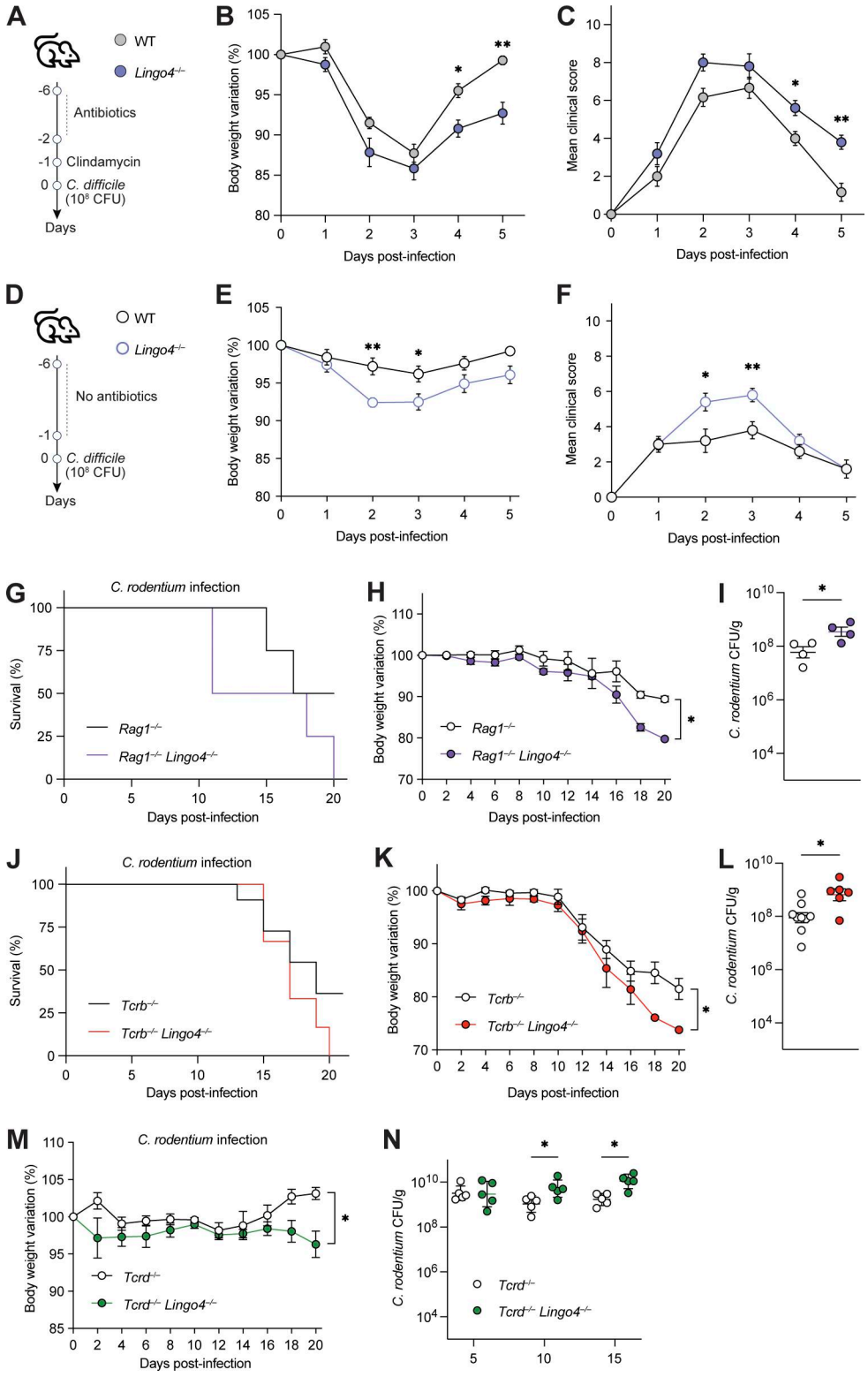

Figure S4. ***Lingo4* deficiency increases susceptibility to *C. difficile* and *C. rodentium* (related to Fig. 4). (A–C)** *C. difficile* infection (CDI) model schematic and outcomes: mice received 4-day antibiotic cocktail followed by i.p. clindamycin and infection with 10^8 *C. difficile* (A); body weights (B) and clinical scores (C). Mean ± SEM, *n* = 8; two experiments combined. **(D–F)** CDI without antibiotic pretreatment (D), body weights (E), and clinical scores (F). Mean ± SEM, *n* = 8; two experiments combined. **(G–I)** Survival (G), body weight (H), and *C. rodentium* burden at 10 d.p.i. (I) in WT and *Lingo4*$^{-/-}$ mice on *Rag1*$^{-/-}$ background. Mean ± SEM, *n* = 4; representative of two experiments. **(J–L)** Survival (J), body weight (K), and *C. rodentium* burden at 10 d.p.i. (L) in WT and *Lingo4*$^{-/-}$ mice on *Tcrb*$^{-/-}$ background. Mean ± SEM, *n* = 6–9; two experiments combined. **(M and N)** Body weight (M) and *C. rodentium* burden at 5, 10, and 15 d.p.i. (N) in WT and *Lingo4*$^{-/-}$ mice on a *Tcrd*$^{-/-}$ background. Mean ± SEM; *n* = 5; representative of two experiments. **(A–N)** Statistical significance was assessed using unpaired two-tailed *t* tests or one-way ANOVA with Tukey's post hoc test. *P < 0.05; **P < 0.01.

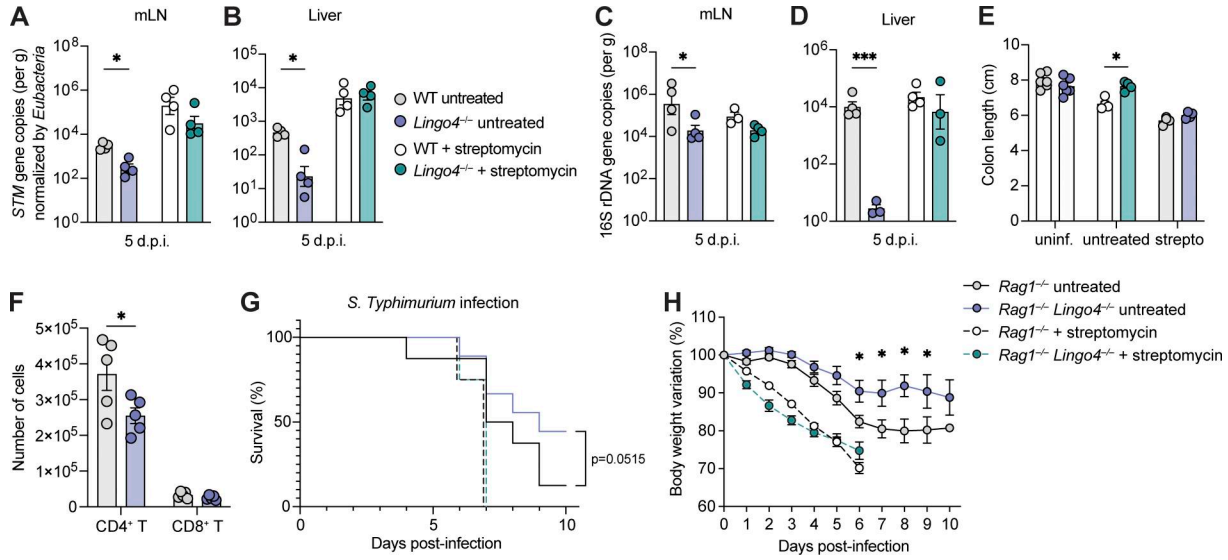

Figure S5. ***Lingo4* deficiency enhances host resistance to *S. typhimurium* infection (related to Fig. 5). (A and B)** *S. typhimurium* burden at 5 d.p.i. in mLN (A) and liver (B), normalized to Eubacteria 16S rRNA gene copies. Mean ± SEM, *n* = 4; representative of two experiments. **(C and D)** Eubacteria 16S rRNA gene copies in mLN (C) and liver (D) at 5 d.p.i. Mean ± SEM, *n* = 4; representative of two experiments. **(E)** Colon length of WT and *Lingo4*$^{-/-}$ mice at 5 d.p.i. Mean ± SEM, *n* = 6; two experiments combined. **(F)** Numbers of CD4$^+$ and CD8$^+$ T cells in siLP of WT and Lingo4$^{-/-}$ mice at 5 d.p.i. Mean ± SEM, *n* = 5; representative of two experiments. **(G and H)** Survival (G) and body weight variation (H) of WT and *Lingo4*$^{-/-}$ mice on *Rag1*$^{-/-}$ background during *S. typhimurium* infection with or without streptomycin pretreatment. Mean ± SEM, *n* = 8–9; two experiments combined. **(A–H)** Statistical significance was assessed using one-way ANOVA with Tukey's post hoc test. *P < 0.05; ***P < 0.001. mLN, mesenteric LN.

Provided online is Table S1. Table S1 lists proteins identified by mass spectrometry following anti-FLAG immunoprecipitation of LINGO4, highlighting interactors enriched in LINGO4-expressing cells compared with control 293T cells.